Systems/Circuits

Basic Properties of Coordinated Neuronal Ensembles in the Auditory Thalamus

Congcong Hu,[1,2,3] Andrea R. Hasenstaub,[1,2,3] and Christoph E. Schreiner[1,2,3]
[1]John & Edward Coleman Memorial Laboratory, [2]Neuroscience Graduate Program, and [3]Department of Otolaryngology-Head and Neck Surgery, University of California-San Francisco, San Francisco, California 94158

Coordinated neuronal activity has been identified to play an important role in information processing and transmission in the brain. However, current research predominantly focuses on understanding the properties and functions of neuronal coordination in hippocampal and cortical areas, leaving subcortical regions relatively unexplored. In this study, we use single-unit recordings in female Sprague Dawley rats to investigate the properties and functions of groups of neurons exhibiting coordinated activity in the auditory thalamus—the medial geniculate body (MGB). We reliably identify coordinated neuronal ensembles (cNEs), which are groups of neurons that fire synchronously, in the MGB. cNEs are shown not to be the result of false-positive detections or by-products of slow-state oscillations in anesthetized animals. We demonstrate that cNEs in the MGB have enhanced information-encoding properties over individual neurons. Their neuronal composition is stable between spontaneous and evoked activity, suggesting limited stimulus-induced ensemble dynamics. These MGB cNE properties are similar to what is observed in cNEs in the primary auditory cortex (A1), suggesting that ensembles serve as a ubiquitous mechanism for organizing local networks and play a fundamental role in sensory processing within the brain.

Key words: **auditory cortex; auditory thalamus; ensemble; rat; synchrony**

Significance Statement

Temporal coordination of neuronal activity has been widely observed in various cortical areas and has been shown to be important for signal processing and information transmission in the brain. However, it remains unclear whether neuronal coordination is exclusive to cortical local networks or if it also holds significance in subcortical regions. We conducted single-unit recordings to investigate coordinated neuronal ensembles (cNEs), which are groups of neurons with synchronous firing, in both the auditory thalamus and cortex. We demonstrated the existence of cNEs in the auditory thalamus, which have similar properties to cNEs in the auditory cortex. This provides evidence that subcortical neuronal coordination can serve as a fundamental mechanism for organizing and processing neural signals.

Introduction

The function of coordinated neuronal activity in cognitive processes has long been a subject of interest in systems neuroscience (Konorski, 1948; Hebb, 1949). Initially, such activity was difficult to observe experimentally. However, recent technological advancements in large-scale recording, such as two-photon imaging and high-density multichannel probes, have facilitated extensive investigations into the properties and functions of coordinated neuronal firing, primarily within the hippocampus and neocortex (Laubach et al., 2000; Baeg et al., 2003; Harris et al., 2003; Bizley et al., 2010; Buzsáki, 2010; Bathellier et al., 2012; Oberto et al., 2022; Boucly et al., 2022; Domanski et al., 2023). These studies have revealed temporal coordination among neurons in several brain areas, shedding light on their potential roles in various cognitive processes, such as perception, memory formation, and decision-making. Indeed, neuronal ensembles have been proposed as the fundamental units for information processing and transmission (Buzsáki, 2010; Yuste, 2015).

In sensory systems in particular, temporal coordination among neurons has been proposed as a mechanism to enhance information processing (Kreiter and Singer, 1996; Dan et al., 1998; See et al., 2018, 2021) and facilitate communication within and between brain regions (Zandvakili and Kohn, 2015; Oberto et al., 2022). Neuronal coordination allows more reliable and specific representation of stimuli (See et al., 2018, 2021; Yoshida

Received Sept. 13, 2023; revised March 4, 2024; accepted March 11, 2024.
Author contributions: C.E.S. designed research; C.H. and C.E.S. performed research; C.H., A.R.H., and C.E.S. analyzed data; C.H. wrote the paper.
We thank Drs. Jermyn See and Natsumi Homma for their help with software and data collection. This work was supported by the National Institutes of Health (DC002260 and DC017396 to C.E.S. and DC014101, NS116598, MH122478, and EY025174 to A.R.H.), the Klingenstein Foundation (A.R.H.), PBBR Breakthrough Fund (A.R.H.), the Coleman Memorial Fund (A.R.H., C.E.S.), and Hearing Research (C.E.S., A.R.H).
The authors declare no competing financial interests.
Correspondence should be addressed to Christoph E. Schreiner at christoph.schreiner@ucsf.edu.
https://doi.org/10.1523/JNEUROSCI.1729-23.2024

and Ohki, 2020; Ebrahimi et al., 2022), and considering neuronal coordination allows identification of emergent stimulus-encoding properties (deCharms and Merzenich, 1996; Shahidi et al., 2019). Additionally, elevated coordination in neuronal activity in an output or sender area often precedes activity in a target or receiver area (Zandvakili and Kohn, 2015). Thus, it is crucial to investigate the expression of coordinated neuronal ensemble (cNE) structure and function at various stages along the sensory pathway.

In the auditory system, A1 contains pairs of neurons with correlated activity (Brosch and Schreiner, 1999; Eggermont, 2000; Atencio and Schreiner, 2013) as well as larger groups of neurons with correlated firing. These groups contribute to the representation of auditory stimuli (Kreiter and Singer, 1996; Miller and Recanzone, 2009; Ince et al., 2013; See et al., 2018). While the characteristics of coordinated activity within the cortex have recently been studied (Bathellier et al., 2012; Chamberland et al., 2017; See et al., 2018, 2021), our understanding of the organization and functional significance of neuronal ensembles in subcortical regions, such as the thalamus, remains unknown. The thalamus is of particular interest since it is the gateway and a direct intermediary between the peripheral sensory system and the cortex (Winer et al., 2005; Smith et al., 2012; Bartlett, 2013). The auditory thalamus, medial geniculate body (MGB), and A1 are highly interconnected, with structured connections linking neurons which share similar spectral and temporal response properties (Miller et al., 2002; Bartlett and Wang, 2007). Considering the strong connections between the thalamus and cortex, investigating the shared characteristics of neuronal ensembles in both regions will help us better understand the role these ensembles may play in auditory information processing and transmission and sensory processing in general.

In this study, we aimed to identify and characterize cNEs in the MGB. We reliably detected cNEs, defined as groups of neurons exhibiting temporally highly coordinated activity, in the MGB. The applied detection method showed robustness, consistently identifying cNEs across different time bin sizes. Importantly, we observed a high degree of similarity between cNEs derived from spontaneous and evoked activity, suggesting that these ensembles represent functional networks that can operate, to a substantial degree, independently of specific sensory stimuli. Furthermore, cNEs in the MGB and A1 shared key characteristics. In both structures, spikes associated with cNEs reflect auditory information more reliably than random spikes from the same neurons. These findings support the hypothesis that cNEs serve as a ubiquitous mechanism for organizing local networks and function as fundamental units for sensory processing in the brain.

Materials and Methods

Animals. All experimental procedures were approved by the Institutional Animal Care and Use Committee at the University of California, San Francisco and followed the guidelines of the National Institutes of Health for the care and use of laboratory animals. Twenty-four female Sprague Dawley rats (wild type, 250–350 g, 2–4 months; RRID:MGI:5651135), sourced from Charles River Laboratories, were used in this study.

Surgery. The detailed procedures were as described in previous studies (See et al., 2018; Homma et al., 2020). Briefly, anesthesia was induced with a combination of ketamine (100 mg/kg, Ketathesia, Henry Schein) and xylazine (3.33 mg/kg, AnaSed, Akorn), along with atropine (0.54 mg/kg, AtroJectSA, Henry Schein), dexamethasone (4 mg/kg, Dexium-SP, Bimeda), and meloxicam (2 mg/kg, Eloxiject, Henry Schein). Additional doses of ketamine (10–50 mg/kg) and xylazine (0–20 mg/kg) were given as needed to maintain anesthesia. Local anesthesia was provided using lidocaine (Lidoject, 2%, Henry Schein) prior to making incisions. The respiratory rate, heart rate, and depth of anesthesia were continuously monitored, and anesthesia was adjusted as needed. The body temperature was monitored and maintained at 37°C using a homeothermic blanket system (Harvard Apparatus 55-7020). Lubricant ophthalmic ointment (Artificial Tears, Henry Schein) was applied to protect the eyes. A tracheotomy was performed to ensure stable breathing during recording. To access the brain, we removed the skin, muscle, skull, and dura over the right temporal lobe, and we applied silicone oil (Sigma-Aldrich) to cover the cortex. A bone rongeur was used to widen the craniotomy window and provide dorsal access to the MGB. A cisternal drain was performed to prevent brain swelling.

Electrophysiology. The frequency organization of auditory cortex was first mapped using tungsten electrodes. A1 was identified as the area with a high- to low-frequency preference gradient on the rostral–caudal axis and short-latency response to pure tones (Polley et al., 2007). Then, electrophysiological recordings were performed using a linear silicon probe with 64 channels (H3, 20 µm channel distance, Cambridge NeuroTech) in the MGB and a two-shank probe with 64 channels (H2, 25 µm channel distance, Cambridge NeuroTech) in A1. The ventral division of the MGB is characterized by a low- to high-frequency gradient on the dorsal–ventral axis (Morel et al., 1987; Anderson and Linden, 2011). The probes were inserted using microdrives (David Kopf Instruments) at a rate of 25 µm/s to a depth of 4,500 to 6,000 µm from the surface of the cortex to reach MGB (Fig. 1*A*) and 900 to 1,300 µm in A1 along the columnar structure (Fig. 7*A*), respectively. Extracellular voltage traces were recorded at a sampling rate of 20 kHz with an Intan RHD2132 Amplifier system (Intan Technologies). Multiunit (MU) activities (Figs. 1*A*, 7*A*) were defined as negative peaks crossing four standard deviations from the mean in the extracellular voltage trace filtered between 300 and 6,000 Hz. Single-unit activities were obtained by spike sorting using Kilosort 2.5 (Steinmetz et al., 2021; Pachitariu et al., 2023), followed by manual curation using Phy (https://github.com/cortex-lab/phy). In the manual curation process, we visually evaluated individual clusters by examining autocorrelograms, spike waveforms, the stability of spike amplitude over time, the persistence of activity over time, the cluster's separation from noise in the feature space, and other visual aids provided by Phy2 for distinguishing single-unit (SU) clusters from MU or noise clusters. Subsequently, the identified units underwent filtering based on specific criteria: interspike interval (ISI) violation within 2 ms <1.5%. The majority of SUs exhibited an ISI violation <0.25%; peak signal-to-noise ratios (SNRs) of the waveform >1.5 (median peak SNR, MGB, 4.52; A1, 3.77); and firing rates >0.1 Hz to eliminate potential MUs. To assess the reliability of activity of the SUs across the entire recording duration, we obtained the presence ratio. This is the ratio of the number of blocks where the unit showed the activity and the total number of blocks in a recording session. To calculate the presence ratio, we divided the entire recording into 100 equal time blocks. The majority of the obtained SUs were active in >95% of the time blocks. This sorting resulted in SUs that exhibit low ISI violations, high peak SNR, firing rates with a log-normal distribution, and a more consistent presence during recording when compared with all clusters generated by Kilosort. To identify oscillatory response in MGB or A1, SUs on the same electrode were combined to form MUs (Fig. 8).

Stimuli. To measure frequency tuning, we presented pure tones with frequencies ranging from 0.5 to 32 kHz in 0.13 octave steps and sound levels from 0 to 70 dB in 5 dB steps (50 ms, 5 ms ramps). Each frequency–sound level combination was presented once in a pseudorandom order, with an interstimulus interval of 250 ms. To assess the spectrotemporal receptive fields (STRFs), we used a 15 min dynamic moving ripple (DMR; Escabí and Schreiner, 2002). The DMR consisted of 40 sinusoidal carrier frequencies per octave in the range of 0.5–40 kHz, each with a random phase. The carriers were slowly modulated (maximum rate of change ≤3 Hz) by a spectrotemporal envelope with a maximum spectral modulation rate of 4 cycles/octave, a maximum temporal modulation rate of 40 cycles/s, and a maximum modulation depth of 40 dB. The mean intensity of the DMR was set at 70 dB sound pressure level. We

selected DMR as the stimulus for analyzing cNEs' response to sound stimuli, as overt onset response effects for the 15 min continuous stimulus are negligible. Additionally, DMR has been observed to reduce oscillatory states in the neural population (Miller and Schreiner, 2000). All auditory stimuli were generated using MATLAB (MathWorks) and calibrated using a 0.5 in pressure-field microphone (Type 4192, Bruel and Kjær). The stimuli were delivered contralaterally from the recording site using a closed-field electrostatic speaker (EC1, Tucker-Davis Technologies) at a sampling rate of 96 kHz.

Detecting cNEs. To identify groups of neurons that exhibit synchronized coactivation, referred to as "cNEs," we used a method combining principal component analysis (PCA) and independent component analysis (ICA; Lopes-dos-Santos et al., 2013; See et al., 2018). We selected a bin size of 10 ms as a standard synchronization span because it represents the most appropriate time window to capture the synaptic integration window of most cortical neurons (Léger et al., 2005; D'amour and Froemke, 2015). First, the individual spike trains of simultaneously recorded neurons were binned and z-scored. Next, the z-scored spike matrix underwent PCA to obtain the eigenvalues of the spike train correlation matrix. To determine the number of cNEs, we took eigenvalues to be significant if their value exceeded the 99.5th percentile of the Marchenko–Pastur distribution, which describes the probability density function of eigenvalues of large rectangular random matrices (Marchenko and Pastur, 1967; See et al., 2018; Fig. 2*A-ii*). We then performed ICA (FastICA) on the subspace spanned by the eigenvectors corresponding to the significant eigenvalues. The resulting independent components (ICs) represent groups of neurons with shared spiking events. The weight of each neuron on an IC indicates the neuron's contributions to the cNE (Fig. 2*A-iii*). As the signs of IC weights were arbitrary, for each IC, the direction with the largest absolute weight was rendered positive. The length of each IC was normalized to one, making an IC with equal contribution from all neurons have weights of $1/\sqrt{N}$, where N was the number of neurons in the recording. Neurons with weights over $1/\sqrt{N}$ were referred to as "cNE members" (Oberto et al., 2022; Fig. 2*A-iv*).

The strength of the cNE activation at each time point was measured by the similarity between the activity of cNE members and the cNE pattern, that is, which neurons in a penetration were cNE members. The similarity can be measured as the square of the weighted sum of the z-scored spike counts, $s = z^T w w^T z = z^T P z$, where z is the z-scored spike counts of cNE members at each time point, w is the IC weights of cNE members, and the projection matrix P is the outer product of w. To consider only the coactivation of multiple cNE members, we set the diagonal of the projection matrix to zero and obtained the modified projection matrix P^*. cNE activity strength was calculated as $s = z^T P^* z$. A null distribution of cNE activity was obtained by projecting a circularly shifted spike matrix, where the temporal relationship of neurons was disrupted, to the template matrix (See et al., 2018). This process was iterated 50 times, and the threshold of cNE activation was defined as the 99.5th percentile of the null distribution (Fig. 2*A-v*). The spikes of the cNE members within the selected time bin where the cNE was active were referred to as "cNE spikes."

Matching cNEs across different bin sizes. We used the correlation between IC weights of all neurons in a penetration to assess the similarity of cNE patterns across different synchronization windows (i.e., time bin width, 2, 5, 10, 20, 40, 80, and 160 ms). To visualize the similarity of cNEs identified using 10 ms bins to those identified using other bin sizes, we calculated the cNEs for the same recording using other bin sizes. We displayed the cNEs whose IC weights were best correlated with the 10 ms cNE (Fig. 3*A*). To measure the variability of cNE identities across bin sizes (Fig. 3*B*,*C*), we matched each cNE to the most similar cNE calculated using reference bins (i.e., when using 10 ms as the reference bin size to the 10 ms cNE which had the best-correlated IC weights). The proportion of shared members with a reference cNE was then calculated by dividing the number of members in a cNE that were also identified as members in its matching reference cNE by the total number of unique members in both cNEs combined.

The significance of the match was determined based on the null distribution of IC weight correlations between matched cNEs. For example, to determine the significance of the correlation between the IC weights of a 10 ms cNE with its most correlated 160 ms cNE, we first generated a null distribution of IC weight correlations. We circularly shifted the spike trains and then applied PCA/ICA to identify sham cNEs using the shuffled spike matrices binned at 160 ms, maintaining the same number of cNEs as the original 160 ms cNEs. Then we identified the most correlated sham 160 ms cNE for the 10 ms cNE. This process was repeated 1,000 times to generate the null distribution of correlation values. The significance threshold was set at $p < 0.01$.

Assessing stability of cNEs. To assess the stability of cNEs during and across spontaneous and stimulus-driven activity, we compared the cNEs from adjacent recording segments (Fig. 4*A*). To match the IC weights of cNEs identified from the different recording segments, we used an iterative process that involved selecting the cNE pairs from the two segments with the highest correlations (Spearman's r; Oberto et al., 2022). First, we computed the correlations between all possible pairs of cNEs that were generated from the two segments. Then, the pair with the highest correlation was set aside, and the same process was repeated with the remaining cNEs until all cNEs were paired. If there were any remaining cNEs that did not have a match due to a difference in the number of cNEs between the two segments, they were left unmatched.

To generate a null distribution of IC weight correlations between matched cNEs from two recording segments (Fig. 4*D*), we circularly shifted spike trains within each activity block. We then applied PCA/ICA to identify sham cNEs using the resulting shuffled spike matrices. As the shuffling disrupted correlations between neurons, very few eigenvalues exceeded the upper bounds of the Marchenko–Pastur distribution. To address this, we maintained the number of sham cNEs in the shuffled data equivalent to the number of significant eigenvalues obtained from the original spike matrix. The sham cNEs from adjacent activity blocks were then matched following the procedure described above. This iterative process was repeated 1,000 times to establish a null distribution of IC weight correlations for the matched cNEs. The 99.5th percentile of each null distribution was set as the significance threshold.

False-positive detection of cNEs. To assess the potential for false-positive cNE detection, we applied the cNE detection algorithm to shuffled data, using the same criteria as those applied to the real dataset. This process was repeated 10 times, resulting in an average count of false-positive cNEs across the circularly shifted data (Fig. 4*F*). Despite conducting 10 iterations, false-positive cNEs were not consistently identified in the neighboring blocks. In cases where a false-positive cNE was detected (i.e., when an eigenvalue computed from shuffled data exceeded the Marchenko–Pastur distribution), we evaluated its stability by measuring the highest correlation of its IC weights with those of real cNEs in the adjacent block (Fig. 4*E*). The significance of false-positive cNE IC weight correlations was determined using the same threshold established for real cNEs.

STRF analysis. For analysis, we downsampled DMR to a resolution of 0.1 octaves in frequency and 5 ms in time. We used the reverse correlation method to obtain the STRFs of the units (Theunissen et al., 2000; Escabí and Schreiner, 2002). To derive the STRFs, we averaged the spectrotemporal envelopes of the stimulus over a period of 100 ms preceding spikes (Figs. 1*B*, 6*A*). Positive (red) values on a STRF indicate that the sound energy at that frequency and time tends to increase the firing rate of the unit, while negative (blue) values indicate where the stimulus tends to decrease the firing rate of the unit. The frequency corresponding to the highest absolute value of the STRF is considered the best frequency (BF) of the unit (Miller et al., 2002). We also determined the peak-to-trough difference (PTD) as a measure of STRF strength.

A STRF was considered significant if it reliably described a neuron's response to DMR sound. To assess the reliability of a STRF, we divided a neuron's spikes into two equal halves and generated two corresponding STRFs (STRF A and B) using each half (Qiu et al., 2003). The similarity

between STRF A and B was computed using Pearson's correlation. This process was reiterated 1,000 times, and the average STRF similarity across these iterations was used as the measure of reliability. To determine the statistical significance of a STRF's reliability, we constructed a null distribution by reversing the neuron's spike train, thus disrupting the temporal correlation of neural responses to the stimulus. We considered STRFs with a reliability surpassing a z-score of 2.58 to be significant.

We used mutual information (MI) as the metric to quantify the amount of information we can obtain about the stimulus by observing spikes of neurons or cNEs (Atencio and Schreiner, 2008; See et al., 2018). The stimulus segment s preceding each spike was projected onto the STRF via the inner product $z = s \times \text{STRF}$.The projection values were then binned to get the probability distribution $P(z|\text{spike})$. The a priori distribution of stimulus projection values, $P(z)$, was calculated by projecting all stimulus segments of DMR onto the STRF, regardless of spike occurrence. Both distributions $P(z)$ and $P(z|\text{spike})$ were normalized relative to the mean μ and standard deviation σ of $P(z)$, by $x = ((z - \mu)/\sigma)$, resulting in $P(x)$ and $P(x|\text{spike})$. The MI between STRF projection values and single spikes was computed according to the following:

$$I = \int dx P(x|\text{spike}) \log_2 \frac{P(x|\text{spike})}{P(x)}.$$

STRF comparisons between cNEs and non-cNE groups of neurons. To control the potential influence of population synchrony on a cNE due to independent neuron activity, we compared STRFs derived from cNEs and non-cNE groups of neurons. If less than half of the members had significant STRFs, the cNE was excluded from analysis.

First, we compared the group STRFs of cNEs and non-cNE groups of neurons (Fig. 6*B-ii*,*C-ii*; See et al., 2018). The group STRF was calculated using all spikes from neurons within a group. To generate non-cNE groups of neurons relative to a cNE, we first selected one neuron from the cNE and then sampled from the remaining neurons with significant STRFs within a penetration, forming a group with the same number of neurons as the cNE for comparison. This process excluded other member neurons of the cNE. This procedure was repeated for all members of the cNE, generating all possible combinations of neurons, each including exactly one member neuron from the cNE under examination. Combinations of neurons that included more than one neuron from any other cNEs in the same recording were then also excluded. For each cNE/non-cNE group comparison, we subsampled the spikes in the cNE and the non-cNE groups to the same number. Subsequently, STRF PTD and MI of the cNE group were compared with the median values of the non-cNE groups.

We also compared the STRFs of cNE spikes with those of coincident spikes from a single neuron (Fig. 6*B-iii*,*C-iii*) to assess the influence of random coincidence on stimulus preference. To obtain coincident spikes from a specific neuron, we first sampled neurons from the recorded population that do not share membership with the neuron under examination in any cNE to create a non-cNE group. We kept the number of neurons in the non-cNE group the same as the cNE to which the neuron being examined belongs. This sampling process was restricted to neurons exhibiting significant STRFs. The coincident spikes of the cNE member refer to spikes within 10 ms of spikes from other neurons within the non-cNE group. We repeated this procedure to generate all possible combinations of non-cNE groups, each containing the cNE member and excluding any neuron that shares membership with the neuron under scrutiny. Coincident spike trains with <100 events were discarded. For each cNE spike/non-cNE spike comparison, we subsampled the cNE spikes and spikes from the non-cNE groups to the same number. Subsequently, the cNE spike STRF PTD and MI were compared with the median values of the random spike STRF PTD and MI from the non-cNE groups.

Quantifying slow oscillations in neural activity. To determine whether the neural activity in a recording showed a prominent pattern of slow oscillations, we measured silence density and the coefficient of variation (CV) of MU firing rate. Silence density was defined as the fraction of 20 ms time bins with no population activity (zero spikes; Mochol et al., 2015). The CV of MU firing rate was calculated as $CV = \sigma/\mu$, where μ is the mean firing rate and σ is the standard deviation of the firing rate binned at 20 ms time bins.

Permutation test. We used permutation tests to determine the statistical significance of differences in cross-correlograms (CCGs) among neurons based on their membership (Figs. 2*C*, 3*D*), as well as to assess differences in the proportion of stable cNEs between different stimulus conditions (Figs. 4*E*, 7*E*). For example, to assess the difference in CCGs between member pairs and nonmember pairs (Fig. 2*C*), we shuffled the membership labels of the CCGs and calculated the difference between the average CCGs of member and nonmember pairs. We repeated this process 10,000 times to generate null distributions of the CCG difference for each data point. The 0.5th and 99.5th percentiles of the null distribution were taken as the cutoffs for significance. We considered consecutive time bins ~0 ms lag with $p < 0.01$ to be significant. To assess the difference in the proportion of stable cNEs, we shuffled the stimulus condition label [spontaneous ("spon"), DMR ("dmr"), or cross-condition comparison ("cross")] and repeated this process 10,000 times to generate a null distribution of the difference in proportion. The significance level was then determined based on the null distribution.

Statistics. Statistical analyses were performed in Python. To compare two unpaired groups (e.g., Fig. 2*B*), we used Mann–Whitney U tests. To compare two paired groups (e.g., Fig. 4*F*), we used Wilcoxon signed-rank tests. Permutation tests (e.g., Fig. 2*C*) and Monte Carlo methods (e.g., Fig. 4*D*) were used as described above. To determine if two samples are drawn from the same distribution, we used Kolmogorov–Smirnov test (Fig. 3*D*). The specific applications of these tests are explained in the results section and figure legends. Significance levels are noted as n.s. ($p \geq 0.05$), * ($p < 0.05$), ** ($p < 0.01$), and *** ($p < 0.001$).

Results

Auditory responses in MGB

We conducted extracellular recordings in the rat MGB (Fig. 1*A*) using a 64-channel linear probe, which allowed us to cover most of its span along the dorsal–ventral axis. To obtain the tonal response properties of the recording sites, we presented pure tones of various frequencies and intensities. In the MGB, we usually observed a gradient in the frequency preference of MU responses from low to high along the dorsal–ventral axis, which could vary gradually (Fig. 1*A-i*) or abruptly (Fig. 1*A-ii*) depending on the probe's location. Responses on most channels in the tonotopic region exhibited clear frequency tuning (between the red lines in Fig. 1*A*), which likely reflect activities in the ventral MGB, the primary input station to the A1. We included all SUs from the MGB in our analysis after spike sorting, without distinguishing between subregions although the vast majority was likely from the ventral nucleus according to its tonotopic organization.

To estimate the STRFs of SUs, we used a 15 min DMR stimulus, which is a broadband noise with varying spectral and temporal modulation (Escabí and Schreiner, 2002). The STRFs of MGB neurons also showed a clear gradient in frequency preference from low to high along the dorsal–ventral axis (Fig. 1*B*), consistent with the MU responses to pure tones. We then examined the firing correlations between pairs of simultaneously recorded SUs. MGB neuron pairs showed widely different correlations in their firing activity, even if they were close in proximity and had similar STRFs. For example, neurons #1, #2, and #3 had similar receptive fields (Fig. 1*B*). While neurons #1 and #3 showed correlated firing in both stimulus-driven and spontaneous activity, neurons #2 and #3

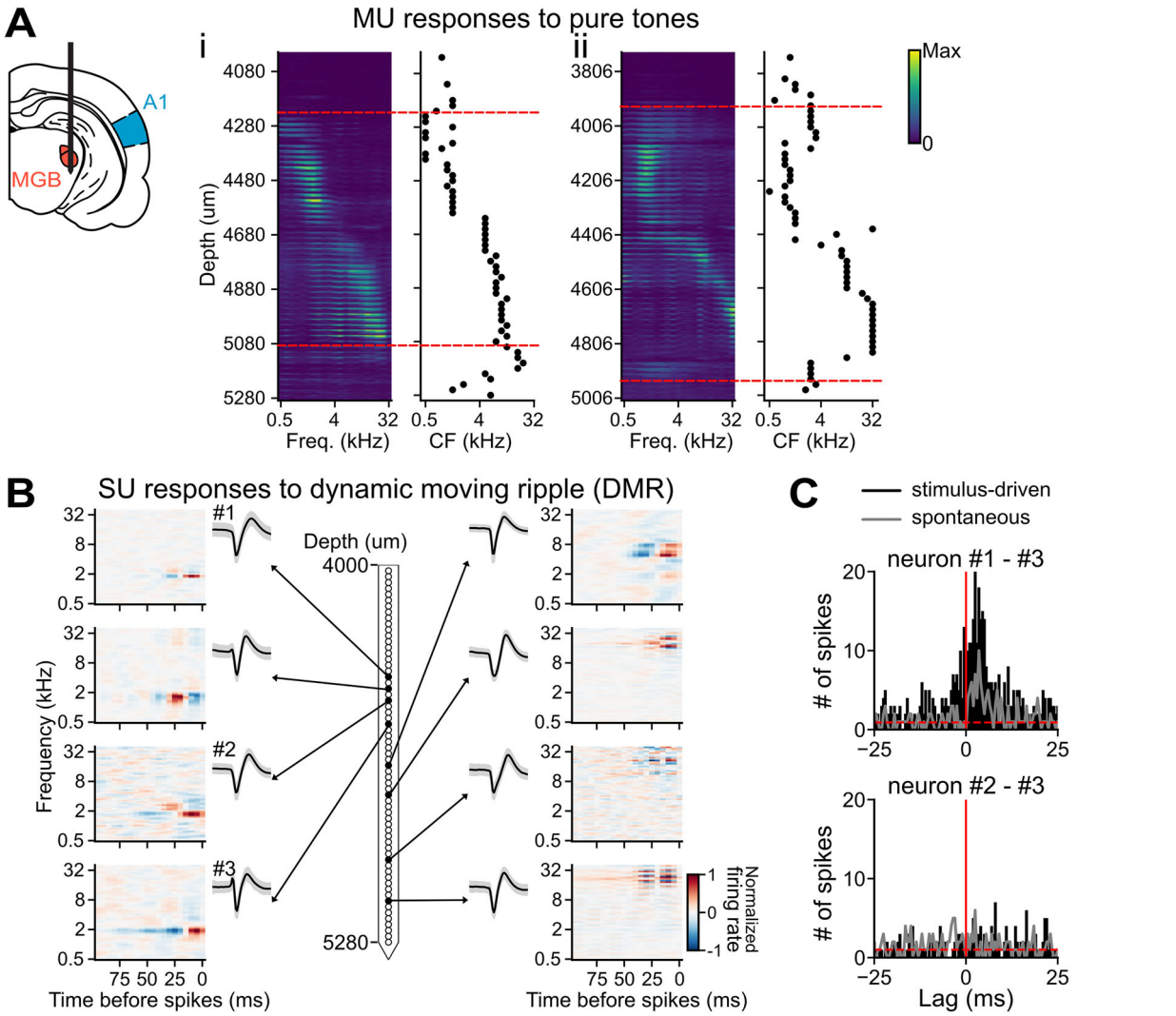

Figure 1. In vivo recordings in rat MGB. ***A***, Left: schematic of the recording setup in the MGB using a linear 64-channel probe. ***i*** and ***ii***, Two electrode penetrations with MU recordings from the MGB. Left: stacked firing rate (color coded) of pure-tone frequency response areas. Right: characteristic frequencies (CF, the frequency at which the response threshold is the lowest). The red dashed lines indicate the potential boundaries of the ventral MGB. ***B***, Example of STRFs of SUs from a recording in the MGB. Unit numbers 1 to 3 indicate the positions and STRFs of pairs of neurons whose CCGs are plotted in ***C***. ***C***, Example CCGs from two pairs of neurons (#1–#3 and #2–#3). The black bars represent the CCGs of stimulus-driven activity, while the gray lines represent the CCGs of spontaneous activity. The baseline is estimated by averaging the counts in 5 ms windows at the shoulders of the CCGs and is indicated by dashed red lines.

showed no significant correlation in their activity despite similar STRFs (Fig. 1*C*). This diversity of correlation patterns, even among neurons with similar receptive fields, parallels what was previously observed in the cortex (Brosch and Schreiner, 1999; Eggermont, 2000; Atencio and Schreiner, 2013; See et al., 2018; Mogensen et al., 2019; Wahlbom et al., 2021). Although the role of neuronal coordination in information processing in the cortex has been extensively proposed and studied (Paninski et al., 2004; Bizley et al., 2010; Buzsáki, 2010; Carrillo-Reid et al., 2015; See et al., 2018), less is known about the organization of neuronal ensembles in subcortical regions. Therefore, we aimed to identify clusters of neurons that exhibit consistent synchronized firing in the MGB and compared the properties of these ensembles with those in A1.

Identifying groups of neurons with coordinated firing in MGB

To identify cNEs, that is, groups of neurons with synchronous firing, we performed a combined PCA–ICA (Lopes-dos-Santos et al., 2013; See et al., 2018). The procedure for detecting cNEs in a population of neurons is demonstrated in Figure 2*A* using a recording of spontaneous activity from the MGB (Fig. 2*A*). Among the 20 isolated SUs in the recording, some pairs of neurons had highly correlated firing with each other, as shown in dark red in the correlation matrix, while others showed low correlation (Fig. 2*A-i*). We performed PCA on the correlation matrix of 10 ms binned spike trains, resulting in 20 eigenvalues and corresponding eigenvectors or principal components (PCs; Fig. 2*A-ii*). These eigenvalues describe the contribution of each PC to the variance in the neural population activity. To determine the significance of the patterns extracted by PCA, we compared the eigenvalues to a threshold drawn based on the Marchenko–Pastur distribution (Peyrache et al., 2010; Lopes-dos-Santos et al., 2013; Fig. 2*A-ii*). In this example recording, we observed four significant eigenvalues above the threshold, indicating the presence of four detectable cNEs in the recorded population. Although PCA efficiently extracts ensemble patterns, it has some limitations due to its variance maximization framework. When two ensembles account for similar variance in the data on their corresponding axis, the first PC will represent the average of the two instead of an individual ensemble.

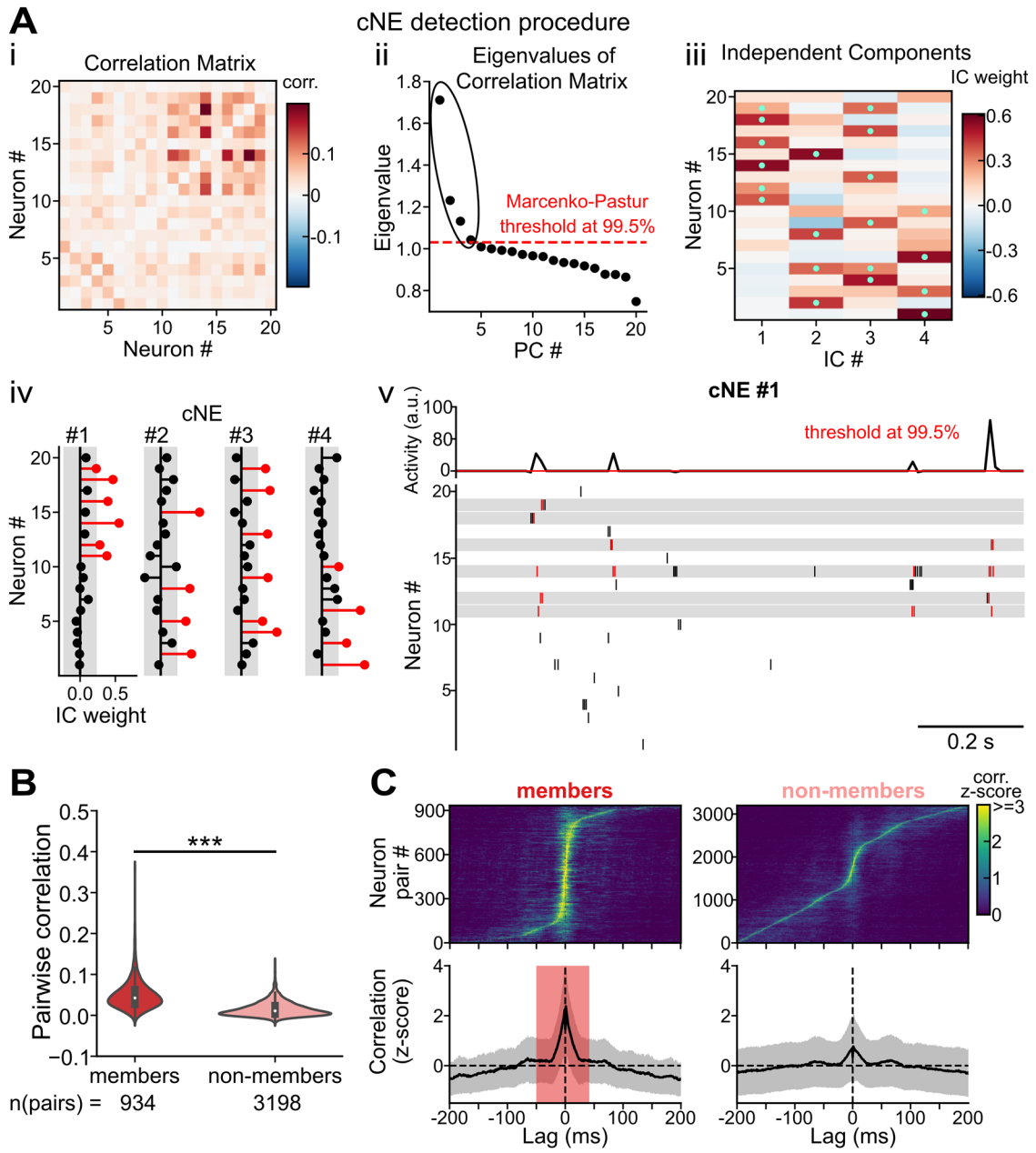

Figure 2. Groups of neurons with coordinated activities exist in MGB. ***A***, Procedures for detecting cNEs in a thalamic penetration. ***i***, Correlation matrix of spike trains. ***ii***, Eigenvalues of the correlation matrix shown in ***i***. The dashed red line represents the 99.5th percentile of the Marchenko–Pastur distribution, which was used as the significance threshold for eigenvalues. The top four eigenvalues are significant and represent the number of detected cNEs. ***iii***, IC weights of neurons for each cNE. The green dots represent neurons that are members of a cNE. ***iv***, cNE members (red stems) are neurons with IC weights exceeding the threshold ($1/\sqrt{N}$) shown as gray areas. ***v***, Example of cNE activation. Top: activity trace of cNE #1. The red line shows the threshold estimated using Monte Carlo methods. The peaks crossing the threshold indicate cNE events when multiple cNE member neurons fire jointly. Bottom: spike raster of neurons, with red ticks indicating spikes that contribute to instances of cNE events, which were referred to as cNE spikes. Shaded areas show member neurons. ***B***, Correlations (10 ms bin) of neuron pairs that were both members of the same cNE (members) and neuron pairs that were not members of the same cNE (nonmembers) in MGB ($p = 6.9 \times 10^{-235}$, Mann–Whitney *U* test). ***C***, *z*-scored CCGs (1 ms bin) of member pairs (left) and nonmember pairs (right) in MGB. Top: stacked CCGs ordered by the peak delay. Bottom: average of the data above (mean ± SD; shaded area, $p < 0.01$; permutation test, shuffling the members/nonmembers labels).

This problem is even more pronounced when ensembles share neurons. To overcome these limitations, we applied ICA to the subspace spanned by the significant PCs (Fig. 2*A-iii*). This approach is not constrained by the orthogonality requirement of PCA, allowing for a more precise identification of individual cNEs. After the PCA–ICA procedure, we obtained the weights of neurons on the axes that define cNEs in the neural population, which were color coded as columns in Figure 2*A-iii*. Neurons were considered members of a cNE if their IC weights were higher than what would be expected from an even weight contribution from all neurons (Fig. 2*A-iv*). The activity resulting from the coactivation of cNE members can be obtained by projecting the spike matrix on the corresponding IC weights of the cNE. To determine the significance of cNE activity magnitude, we generated a null distribution of the cNE activity values by circularly shuffling spike trains and set the significance criteria at 99.5% (Fig. 2*A-v*). For example, when cNE #1 was active, multiple

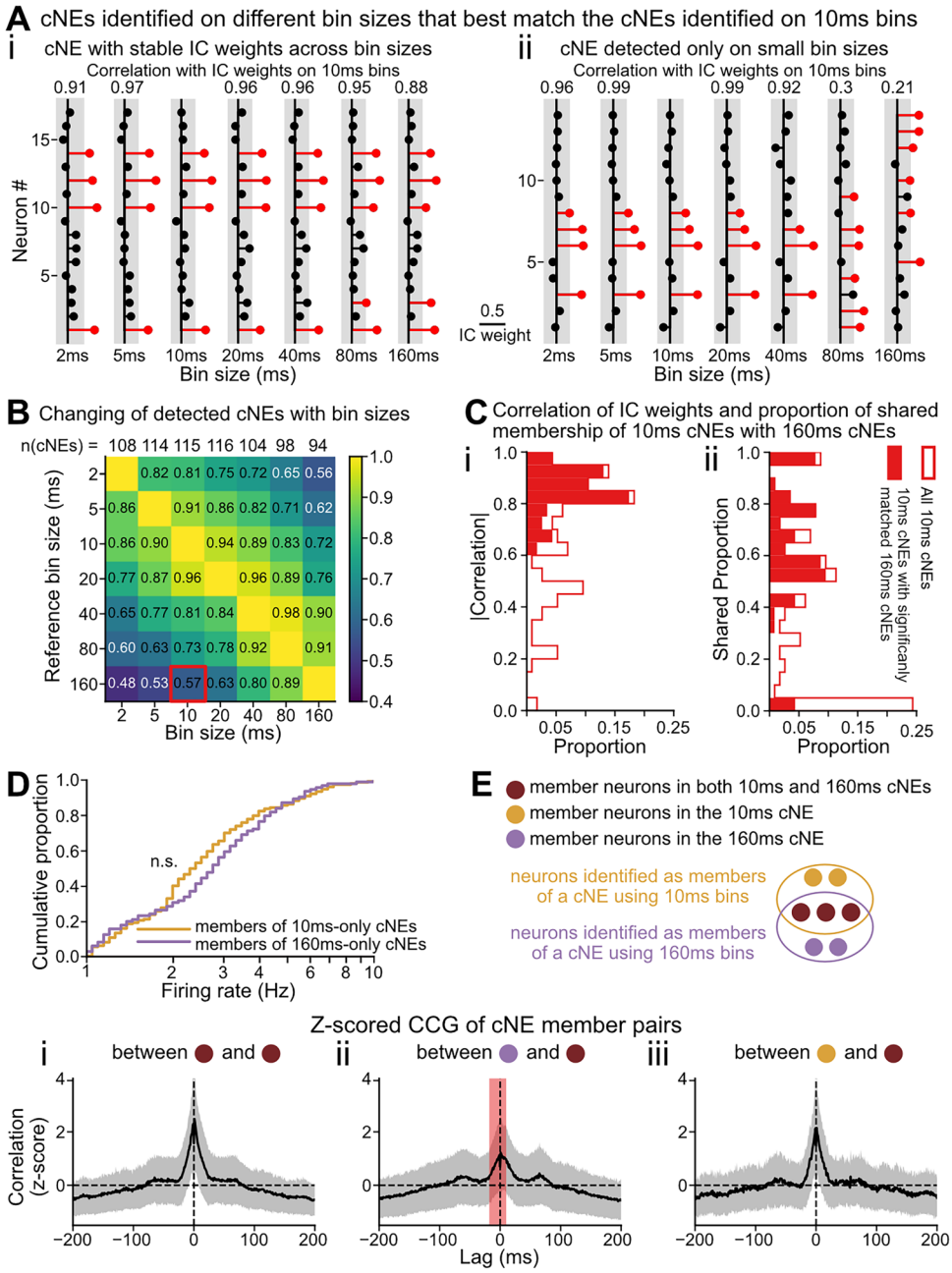

Figure 3. Variability of IC weights across different time bin sizes. ***A***, Example of two MGB cNEs whose member neurons are either consistently identified across different bin sizes (***i***) or only detected using smaller bin sizes (***ii***). ***B***, Proportion of significantly matched cNEs. Using different bin sizes as reference bin sizes (row), we calculated the proportion of cNEs on different bin sizes that have a significantly matched cNE on the reference bin size. The red square highlights the proportion of 10 ms cNEs that have significant matches with 160 ms cNEs and is further analyzed in ***C***. ***C***, Left: correlation of IC weights of 10 ms cNEs with the most correlated IC weights of 160 ms cNEs. Right: proportion of shared membership between 10 ms cNEs with their most correlated 160 ms cNEs. ***D***, Firing rate of member neurons in 10-ms-only cNEs, 10 ms cNEs without a significant match with 160 ms cNEs, and 160-ms-only cNEs ($p = 0.57$; Kolmogorov–Smirnov test). ***E***, Top: schematic of membership of neurons for different bin sizes. Bottom: mean *z*-scored CCGs (1 ms bin, mean ± SD) between (***i***) member neurons in both 10 ms and 160 ms cNEs, (***ii***) member neurons only in the 160 ms cNE and member neurons in both 10 and 160 ms cNEs (shaded area, $p < 0.01$, permutation test, shuffling neuron pair labels of ***i*** and ***ii***), and (***iii***) member neurons only in the 10 ms cNE and member neurons in both 10 and 160 ms cNEs (no time bin showed significant difference from ***i***).

member neurons (2–5 out of 6) fired together. The combined PCA–ICA approach provided a useful framework to investigate the organization and function of coordinated neuronal activity in the MGB.

To provide evidence that cNEs captured groups of neurons with correlated firing, we compared the correlations of 10 ms binned spike trains based on their cNE membership. Pairs of neurons that participated in the same cNE ("member pairs") exhibited significantly higher correlations compared with pairs of neurons that did not share membership in any cNE ("nonmember pairs") (Fig. 2*B*). To examine the correlation between member and nonmember pairs at a finer timescale, we cross-correlated the spike trains using 1 ms bins. The correlation among cNE member pairs was significantly higher compared with nonmember pairs within the [−50, 40] ms lag window (red-shaded area in Fig. 2*C*, bottom left). These results provided evidence that groups of neurons with coordinated firing exist in the MGB and that their coordination was

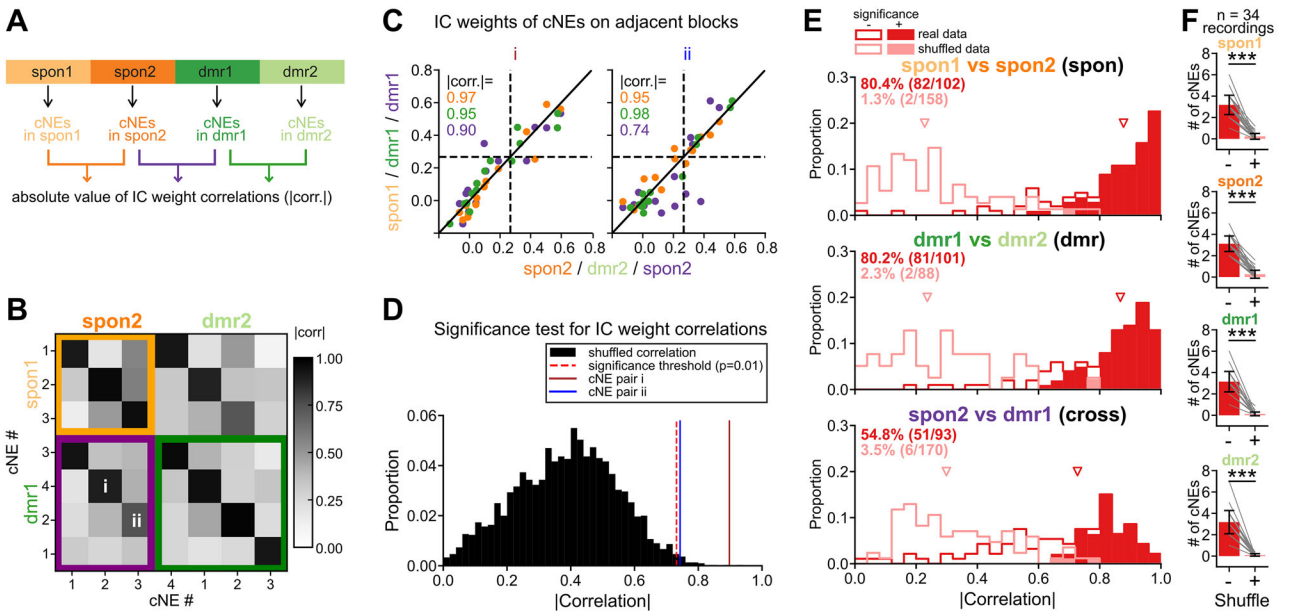

Figure 4. cNEs identified in spontaneous activity are mostly preserved in stimulus-driven activity. ***A***, Diagram illustrating the recording sequence and partitioning of spontaneous (yellow/orange) and DMR-evoked (dark green/light green) activity. The four blocks allowed the comparison of cNEs obtained within stimulus conditions and across stimulus conditions. ***B***, Absolute correlation values of the IC weights calculated on adjacent blocks from an MGB recording including the two examples (***i*** and ***ii***) shown in ***C***. ***C***, Example of IC weights on adjacent blocks with high (***i***) and moderate (***ii***) correlation values across stimulus conditions. The dashed lines show the threshold to determine the membership of the neurons. ***D***, The two cNE examples in ***C*** have significantly matched IC weights across stimulus conditions. See the method for how the null distribution was generated. The significance threshold for the correlation values was set at $p = 0.01$ (red dashed line, 99.5th percentile of the null distribution). The brown (***i***) and blue (***ii***) solid lines represent the two examples in ***C***. ***E***, Correlations of IC weights identified on adjacent activity blocks for real (red) and circularly shifted data (pink). The hollow histograms show all correlations of matched cNEs on adjacent blocks; the histograms show significant correlations based on the test shown in ***D***. The inset numbers show the percentage of cNEs with significantly matched IC weights on adjacent blocks. The triangles show the median of all IC weight correlations (real data vs shuffled data, spon, $p = 5.6 \times 10^{-36}$; dmr, $p = 1.3 \times 10^{-28}$; cross, $p = 2.0 \times 10^{-22}$, Mann–Whitney *U* test with Bonferroni's correction). ***F***, The number of cNEs detected using real and circularly shifted activities on the four recording blocks (spon1, $p = 4.7 \times 10^{-10}$; spon2, $p = 4.7 \times 10^{-10}$; dmr1, $p = 4.7 \times 10^{-10}$; dmr2, $p = 4.7 \times 10^{-10}$; Wilcoxon signed-rank test with Bonferroni's correction).

captured by the PCA–ICA procedure, resulting in the identification of cNEs.

Variability in cNE identity for different bin sizes

The temporal frame used to identify neuronal ensembles plays a critical role in shaping our understanding of their nature and function (Buzsáki, 2010). To investigate how different choices of timescale affect the identification of cNEs, we calculated cNEs using various spike train bin sizes, ranging from 2 to 160 ms (Fig. 3). Some cNEs showed consistent IC weights across different time bin sizes, with a high correlation to IC weights obtained using 10 ms bins (Fig. 3*A-i*). Other cNEs could only be consistently identified using smaller time bin sizes but deviated from those when assessed with larger bin sizes (Fig. 3*A-ii*). We matched cNEs calculated using different bin sizes to evaluate their similarity (Fig. 3*B*). With only small change in the bin size, the cNEs identified were highly similar. For example, 96% of cNEs identified using 10 ms bins had a significant match with 20 ms cNEs. However, when compared with cNEs calculated with larger differences in bin sizes, their identities could vary substantially. For example, 43% of 10 ms cNEs did not show a significant match with 160 ms cNEs (Fig. 3*B*). The remaining 57% of 10 ms cNEs that significantly matched 160 ms cNEs exhibited high correlation (>0.6) in their IC weights (Fig. 3*C-i*). Moreover, the majority of significantly matched cNEs shared more than half of their neuron membership. Nonetheless, ~25% of 10 ms cNEs had no common members with the 160 ms cNEs (Fig. 3*C-ii*). There was no significant difference in the firing rate of MGB neurons participating in 10 ms and 160 ms cNEs (Fig. 3*D*). In summary, small variations in time bin sizes have a limited effect on cNE identity. However, using large time bin sizes to identify cNEs, such as 160 ms, may result in the loss of half or more of the cNEs identified using small bin sizes, such as 10–20 ms.

In cases where differences in cNE membership arise due to different bin sizes, we investigated the firing correlations between neurons that had shifted in or out of the ensemble. We compared the membership of neurons in cNEs identified using 10 ms and 160 ms bin sizes ("10 ms cNEs" and "160 ms cNEs," Fig. 3*E*) and categorized neurons in each cNE as the following: members in both 10 and 160 ms cNEs, members only in the 10 ms cNE, or members only in the 160 ms cNE. Neurons sharing memberships in both 10 and 160 ms cNEs (stable members) had positive correlations in their firing (Fig. 3*E-i*). Neurons only in 160 ms cNEs were positively correlated with stable members, although the correlation was significantly weaker in the [−17, 10] ms window (Fig. 3*E-ii*) compared with the correlation among stable members (Fig. 3*E-i*). Furthermore, some members of 10 ms cNEs were not identified as members in 160 ms cNEs. These neurons showed no significant difference in their correlations with stable members (Fig. 3*E-iii*) compared with the correlation among stable members (Fig. 3*E-i*). Therefore, using wider bin sizes to identify cNEs results in neurons with weak correlations being included in the ensemble, as well as neurons with strong correlations being omitted.

Variability in cNE structures across spontaneous and evoked activity

Several studies have shown that cortical neuronal ensembles have stable structures across spontaneous and stimulus-driven

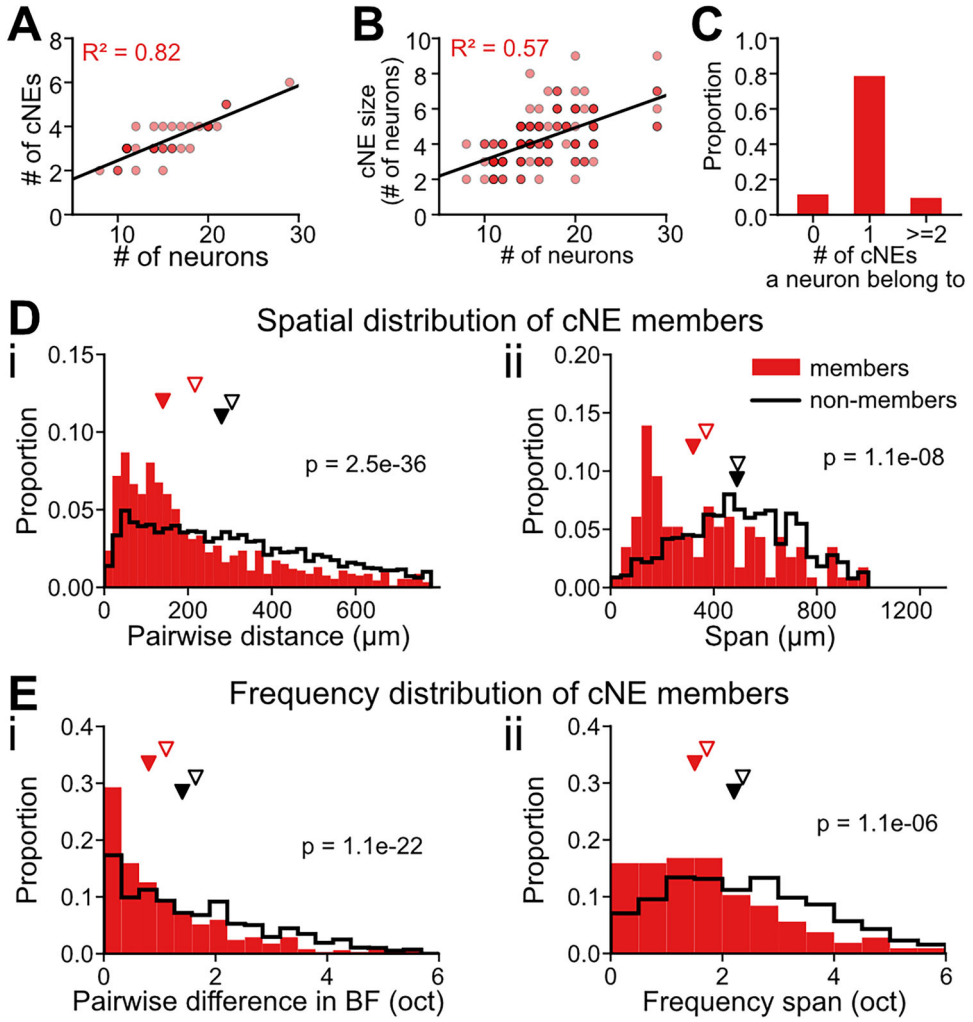

Figure 5. Properties of cNEs in MGB. ***A***, The number of cNEs detected in any given penetration increases with the number of recorded neurons. ***B***, cNE size increases with the number of recorded neurons. ***C***, The number of cNEs a neuron belongs to. ***D***, Spatial distribution of cNE members. ***i***, Pairwise distance of neurons in the same cNE (colored bar) or neurons not in the same cNE (black line). ***ii***, Spatial span of cNE members (colored bar) and random groups of neurons with the same number of neurons as cNEs (black line). ***E***, Frequency tuning distribution of cNE members. ***i***, Pairwise difference in the BFs of neurons. ***ii***, The largest difference in the BF among cNE members or random groups of neurons (Mann–Whitney *U* test).

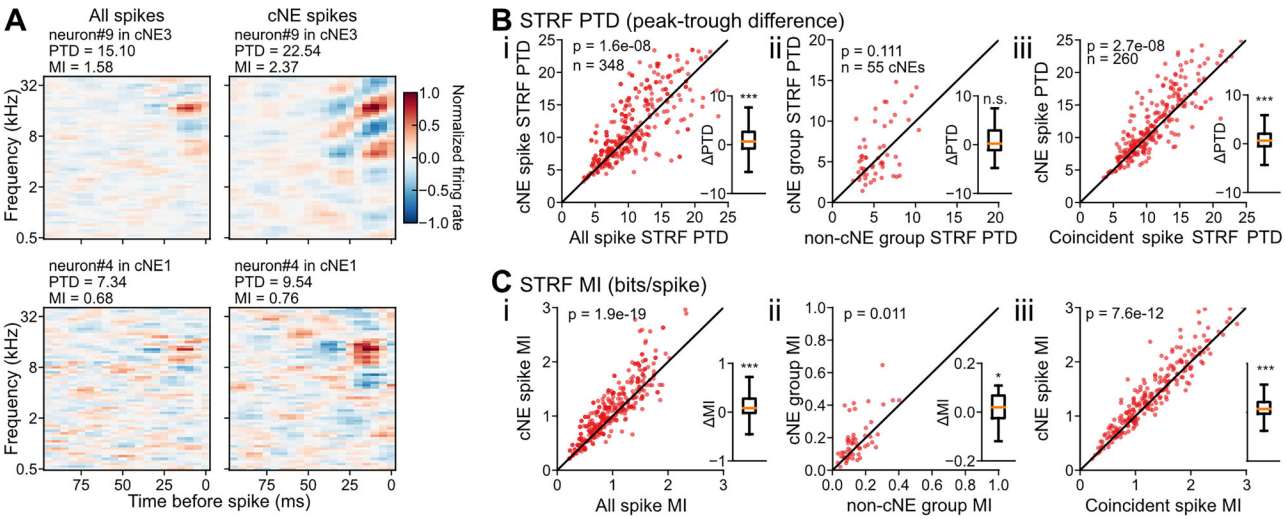

Figure 6. MGB cNEs can refine sound features encoded by member neurons. ***A***, Two examples of STRFs of MGB neurons calculated with all spikes (left) and cNE spikes (right). All spikes are subsampled to have an equal number as cNE spikes. ***B***, ***i***, STRF PTD for cNE spikes or all spikes of neurons. ***ii***, STRF PTD for groups of cNE members or nonmembers. ***iii***, STRF PTD for cNE spikes and coincident spikes of a neuron. The coincident spikes refer to instances where a neuron's firing occurs within a 10 ms timeframe of another neuron's firing in a group of nonmember neurons. This group is designed to match the number of neurons present in the cNE. ***C***, ***i***, MI between stimulus and cNE spikes or all spikes of neurons. ***ii***, STRF MI for groups of cNE members or nonmembers. ***iii***, STRF MI for cNE spikes and coincident spikes of a neuron (Wilcoxon signed-rank test).

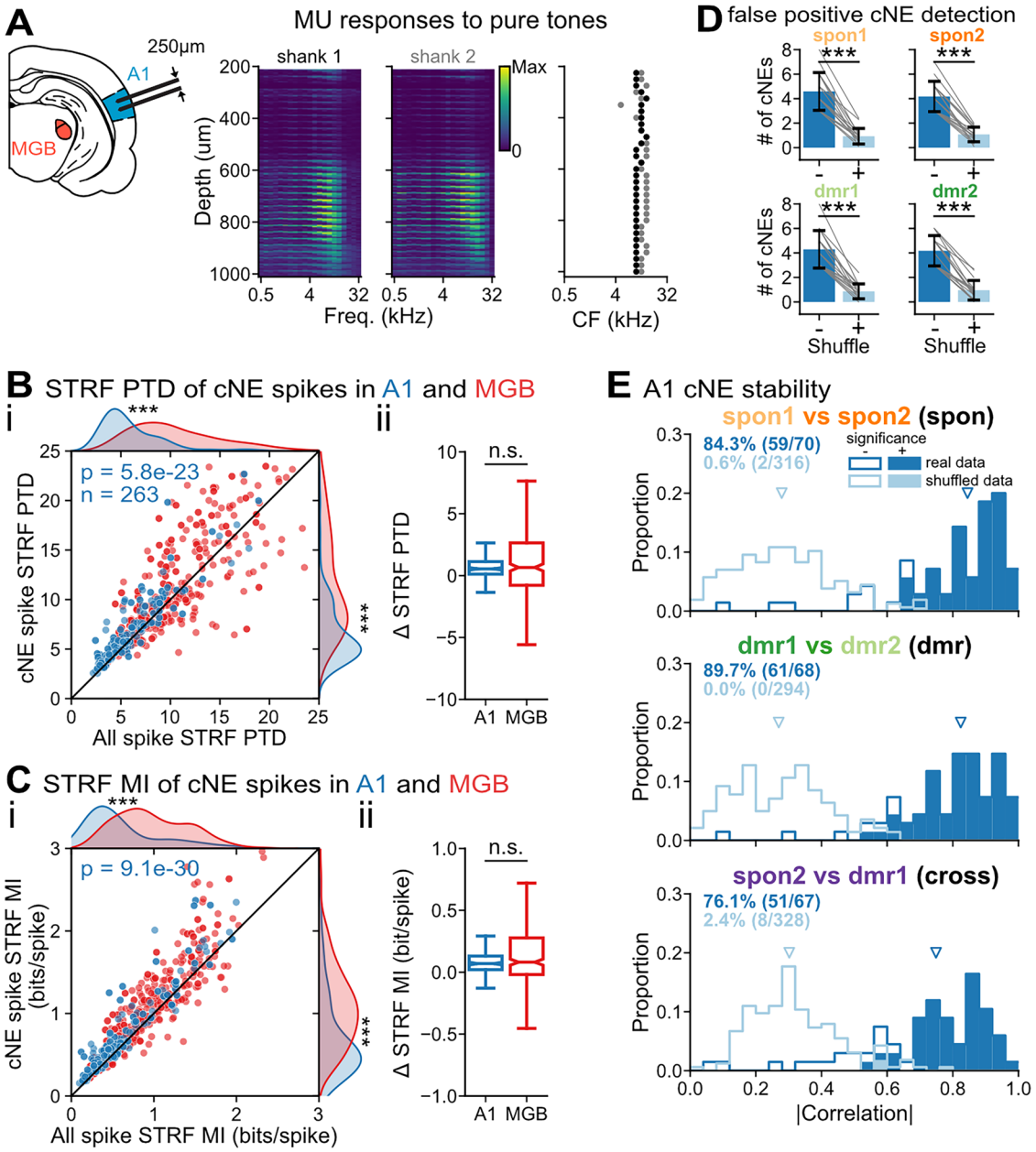

Figure 7. MGB and A1 cNEs have similar properties. ***A***, Left: schematic of the recording setup in A1 using a two-shank probe with 64 channels. Right: MU responses to pure tones as in Figure 1*A*. ***B***, ***i***, PTD of STRFs calculated using all spikes or only cNE spikes from a neuron in A1. ***ii***, Difference between cNE spike STRF PTD and all spike STRF PTD in MGB and A1 ($p = 0.72$, Mann–Whitney *U* test). ***C***, ***i***, MI of STRFs calculated using all spikes or only cNE spikes from a neuron in A1. ***ii***, Difference between cNE spike STRF MI and all spike STRF MI in MGB and A1 ($p = 0.92$, Mann–Whitney *U* test). ***D***, The number of cNEs detected using real and circularly shifted activities on the four recording blocks in A1, as shown in Figure 4*F* for MGB (spon1, $p = 6.1 \times 10^{-5}$; spon2, $p = 6.1 \times 10^{-5}$; dmr1, $p = 6.1 \times 10^{-5}$; dmr2, $p = 6.1 \times 10^{-5}$; $n = 17$ recordings; Wilcoxon signed-rank test with Bonferroni's correction). ***E***, Correlations of IC weights identified on adjacent activity blocks for real (blue) and circularly shifted data (light blue) in A1. The hollow histograms and histograms show the distribution of correlations and significant correlations as in Figure 4*E*. The triangles show the median of IC weight correlations (spon, $p = 1.4 \times 10^{-33}$; dmr, $p = 4.6 \times 10^{-34}$; cross, $p = 4.8 \times 10^{-28}$; Mann–Whitney *U* test with Bonferroni's correction).

activity, suggesting a consistent local network organization utilized in processing stimulus information (Jermakowicz et al., 2009; Luczak et al., 2009; See et al., 2018; Filipchuk et al., 2022). To investigate if this property also exists in cNEs in the MGB, as was observed in A1 (See et al., 2018), we recorded continuous segments of neural activity in the absence of sound ("spon") and during the presentation of the DMR stimulus ("dmr"). We divided each activity type into two segments and detected cNEs in each segment separately. We then compared the stability of the cNEs within and across stimulus conditions, measured by the correlation of IC weights between adjacent segments (Fig. 4*A*,*B*). We observed that while some cNEs exhibited high stability across stimulus conditions, with IC weight correlation comparable to that within the same stimulus condition (Fig. 4*C-i*), others showed structures that were less stable across stimulus conditions compared with within a stimulus condition (Fig. 4*C-ii*). Using null distributions generated by circularly shuffling spikes, we determined the significance of the IC weight correlations and found that both examples in Figure 4*C* were significantly stable across stimulus conditions, although one

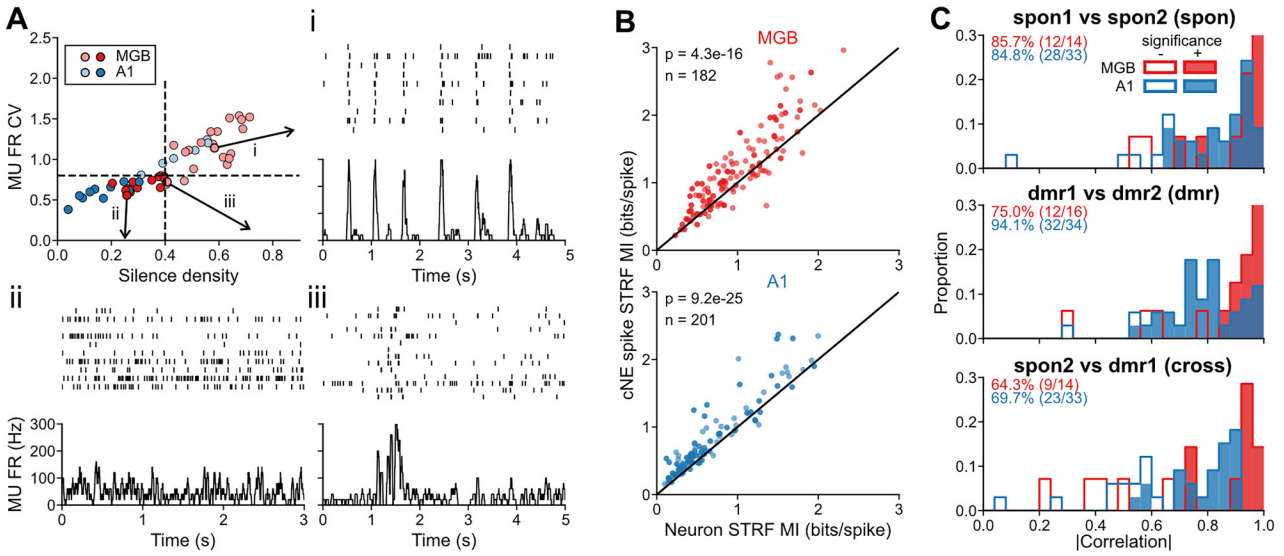

Figure 8. cNE events do not rely on slow oscillation in neural activity. ***A***, Silence density and firing rate (FR) CV of population activity in response to DMR. Some recordings show strong slow oscillation in population activity with pronounced silent period between highly active moments (***i***), while others show little (***ii***) or moderate (***iii***) levels of slow MU firing rate oscillation. Recordings with silence density <0.4 and MU firing rate coefficient of variance <0.8 (dashed lines) did not show prominent slow oscillation in population activity and were included in ***B***. ***B***, STRF MI with all spikes and cNE spikes in recordings without prominent slow oscillations (Wilcoxon signed-rank test). ***C***, Correlation values of cNE IC weights on adjacent activity blocks from recordings with no prominent slow oscillations in both spontaneous and stimulus-driven activities. The inset numbers show the percentage of cNEs with significantly matched IC weights on adjacent blocks in MGB (red) and A1 (blue). The hollow histograms and histograms show all correlation values and significant correlation values with the same presentation scheme as in Figure 4*E*.

was slightly more stable than the other (Fig. 4*D*). In MGB, within spontaneous or stimulus-driven activity, ~80% of cNEs exhibited stable structures across adjacent activity blocks (Fig. 4*E*). Significantly fewer cNEs (54.8%) were stable across stimulus conditions than within a stimulus condition (spon vs cross, $p = 0 \times 10^{-4}$; dmr vs cross, $p = 6 \times 10^{-4}$; spon vs dmr, $p = 1.0$; permutation test with Bonferroni's correction). The results provide evidence for the stability of cNEs in the MGB, during both spontaneous and stimulus-driven activity, although fewer cNEs exhibit stable structures across different stimulus conditions than within the same stimulus condition.

To test the possibility of false-positive detection of cNEs, we generated shuffled data on each segment by circularly shifting spike trains to disrupt their temporal correlations. We then applied the cNE detection algorithm to the shuffled data using the same criteria as for the real data. Our analysis revealed a drastically lower number of cNEs identified in shuffled segments (real data vs shuffled data, spon1, 3.2 ± 0.9 vs 0.2 ± 0.3; spon2, 3.1 ± 0.7 vs 0.3 ± 0.4; dmr1, 3.1 ± 0.9 vs 0.1 ± 0.2; dmr2, 3.2 ± 1.1 vs 0.1 ± 0.1, mean ± SD; Fig. 4*F*), suggesting that the chance of false-positive detection of cNEs is quite low. Furthermore, any cNEs identified in the shuffled data did not exhibit the same stability across stimulus conditions observed in real data (Fig. 4*E*). In summary, our findings indicate that the detection of cNEs in the MGB is reliable and not susceptible to false positives. Moreover, the properties of cNEs we observe, such as their stability across stimulus conditions, are genuine and not artifacts of random data.

cNE properties in MGB

We determined some basic structural properties of MGB cNEs. The spontaneous activity in 34 MGB recordings revealed 115 cNEs with 3.4 ± 0.9 cNEs per penetration. More cNEs were observed in penetrations that captured a higher number of isolated SUs (Fig. 5*A*). The mean cNE size was 4.3 ± 1.5 members, dependent on the number of isolated neurons (Fig. 5*B*). Of the 407 neurons isolated in MGB, the majority (78.6%) belonged to a single cNE, 11.5% did not belong to any cNE, and 9.8% belonged to multiple cNEs (Fig. 5*C*).

Next, we investigated whether cNE members were physically and functionally closer to each other than nonmember pairs of neurons. The pairwise spatial distance of cNE members was significantly smaller than that of nonmember pairs of neurons in MGB (Fig. 5*D-i*). Moreover, the span of cNEs, defined as the longest pairwise distance among all members, was shorter than that of randomly selected groups of neurons in the recording (Fig. 5*D-ii*). The tuning of cNE members was also closer to each other, as the difference in the BF between cNE member pairs was smaller than that of nonmember pairs (Fig. 5*E-i*). The BF span of cNEs, defined as the largest difference in BF among all members, was smaller than that of randomly selected groups of neurons (Fig. 5*E-ii*). Our results demonstrate that cNEs in the MGB are composed of neurons that are physically and functionally closer to each other than nonmember pairs, suggesting a pattern of local circuit organization as well as local functional congruence.

While we observed similarity in the tuning of cNE members (Fig. 5*E-ii*), cNEs are not limited to groups of neurons with similar receptive fields. The distribution of the pairwise difference in the BF of cNE members exhibits a long tail, where cNE members could differ in their BF by >4 octaves (Fig. 5*E-i*). This suggests that neurons with largely different tuning properties also exhibit synchronous activities and participate in the same cNE.

Previous studies have proposed a manifestation of ensemble coding based on neuronal groups with covarying firing rate (Wills et al., 2005; Niessing and Friedrich, 2010; Aschauer et al., 2022), for example, groups of neurons that jointly increased their firing rates in response to various pure tones (Aschauer et al., 2022). Assessing coactivation based on the firing rate in response to various stimuli, however, is a limited basis for the

identification of neurons that functionally cooperate. Such methods may simply reflect coactivation due to the overlap between receptive fields along the tonotopic axis, and distinct groups of neurons may emerge due to BF discontinuities in the tonotopic organization (Fig. 1*A*; Imaizumi et al., 2004). A more stringent criterion, that of tight temporal synchrony, as utilized here, can help differentiate between neuron groups based on coincidental coactivation and groups based on synchronous coactivation.

cNEs enhance stimulus information encoding

Synchronization of neuronal spikes in the cortex has been found to enhance information encoding about a stimulus compared with the participating neurons alone (Dan et al., 1998; Atencio and Schreiner, 2013; See et al., 2018). This is consistent with the multiplexed nature of an individual spike train, whereby spikes representing distinct stimulus aspects are mixed but can be separated based on their synchrony with other neurons (Lankarany et al., 2019; See et al., 2021). To investigate whether spikes from individual neurons that participate in cNEs also exhibit differential coding compared with the neuron's entire spike train, we compared the STRFs calculated using all the spikes emitted by a neuron to STRFs only based on the subset of spikes that contributed to cNE events ("cNE spikes"; Fig. 6*A*). The spike trains were subsampled to ensure an equal number of spikes across conditions. Our analysis revealed that the STRFs of cNE spikes exhibit stronger excitatory and inhibitory fields compared with the STRFs of all spikes from the same neuron, as evidenced by the larger PTD of the cNE STRFs (Fig. 6*B-i*), which quantifies the difference between the largest and smallest value in the STRF. Given that PTD only considers two extreme values in the STRF, we further evaluated the reliability of cNE spikes relative to all spikes in encoding the sound features represented by their STRFs by calculating the MI between the stimulus and the spikes. Our results demonstrate that cNE spike STRFs have higher MI than STRFs constructed from all spikes (Fig. 6*C-i*).

To demonstrate that the increased information conveyed by cNE spike STRFs was not simply because cNEs integrate signals over multiple neurons and thus must enhance information through population encoding, we compared STRFs derived from cNE member and nonmember neurons. First, we compared the MU STRFs of cNE member neurons (cNE group STRF) with those of a neuronal group devoid of neurons sharing membership from any cNE (non-cNE group STRF). The cNE group STRFs exhibited a significantly higher MI than that of the non-cNE STRFs, although no significant difference in PTD was observed (Fig. 6*B-ii*,*C-ii*). As the group STRFs did not take spike synchrony into account, we further compared cNE spikes and coincident spikes of a cNE member. The coincident spikes refer to spikes that occurred within a 10 ms window relative to firing of other neurons not sharing membership with the neuron under examination. Both the PTD and MI of cNE spike STRFs were significantly higher than that of the coincident spike STRFs (Fig. 6*B-iii*,*C-iii*).

Collectively, these findings suggest that cNE spikes can enhance information processing by increasing the SNR and promoting more consistent encoding of certain stimulus features compared with including all spikes from the neuron. Furthermore, the enhanced information encoding of cNEs is not a trivial result of population encoding but rather hinges on the identity of cNE members and synchronous spike events.

MGB and A1 cNEs have similar properties

The properties and functions of cNEs have previously been explored within the primary auditory cortex (A1; See et al., 2018, 2021), whereas investigations into cNEs in subcortical regions are limited. Hence, we aim to determine whether the properties of cNEs in the MGB differ substantially from those observed in A1 cNEs or if they share similarities. To target A1, we used a two-shank probe with 64 channels. The MU responses to pure tones from the two shanks of the probe exhibited similar frequency tuning, as the shanks sampled nearby cortical columns (Fig. 7*A*). The responses on each shank showed small variation in their frequency preference along the depth of the probe, as neurons in the same cortical column have consistent characteristic frequencies across the active middle and deep cortical layers (Atencio and Schreiner, 2010; Merzenich et al., 1975). Much like cNEs in MGB, cNE spike STRFs in A1 exhibited higher PTD and MI compared with all spike STRFs (Fig. 7*B-i*,*C-i*). Compared to A1 neurons, MGB neurons displayed significantly higher STRF PTD (all spike STRF PTD, $p = 3.1 \times 10^{-42}$; cNE spike STRF PTD, $p = 8.6 \times 10^{-36}$) and MI (all spike STRF MI, $p = 1.9 \times 10^{-25}$; cNE spike STRF MI, $p = 4.2 \times 10^{-22}$). We did not observe, however, a significant difference between MGB and A1 cNEs regarding their gain in cNE spike STRF PTD and MI values over that of member neuron spiking (Fig. 7*B-ii*,*C-ii*).

Addressing concerns of potential false-positive detections in A1, we compared the number of cNEs detected on real and shuffled activities. A substantially smaller number of cNEs were detected on shuffled data compared with real data (real data vs shuffled data, spon1, 4.6 ± 1.5 vs 0.9 ± 0.6; spon2, 4.2 ± 1.2 vs 1.1 ± 0.6, dmr1, 4.3 ± 1.5 vs 0.9 ± 0.6, dmr2, 4.2 ± 1.2 vs 1.0 ± 0.8; mean ± SD; Fig. 7*D*). Moreover, A1 cNEs were mostly stable across stimulus conditions, similar to MGB cNEs, whereas false-positive cNEs did not show such stability (Fig. 7*E*). The similarity between MGB and A1 cNEs in their stability across stimulus conditions and enhanced information encoding provides support for the concept of cNEs serving as a universal mechanism for neuronal organization and information processing.

cNE formation does not rely on strong slow oscillations

Slow-wave oscillations, characterized by alternating periods of large and sustained network activity (up states) and neural quiescence (down states), are frequently observed in the cortex and thalamus during anesthesia (Steriade et al., 1993; Contreras et al., 1996; Sanchez-Vives and McCormick, 2000; Hasenstaub et al., 2007; Chauvette et al., 2011; Neske, 2016). To quantify the level of slow oscillations in the recording and their potential influence on cNE properties, we used two measurements: silence density and the CV of the MU firing rate. Silence density represents the proportion of recording time when no spike was fired by the neural population, which is a characteristic of the down state in slow oscillations. In brains without strong slow oscillations, the population of neurons fires continuously, resulting in low silence density. The MU firing rate CV measures the level of variation in the firing rate of the MU, which is high for neurons going through up–down state cycles but small for neural populations with less synchronized oscillatory activity. Recordings with high silence density and high MU firing rate CV showed prominent slow oscillations, with epochs of synchronous firing of neurons and epochs of quiescence with no spikes (Fig. 8*A-i*). In contrast, recordings with low silence density and low MU firing rate CV did not exhibit strong slow oscillations, displaying relatively stable and continuous firing (Fig. 8*A-ii*). Recordings with moderate silence density and MU firing rate CV exhibited moments of elevated firing, although not as synchronized as in recordings with strong oscillations (Fig. 8*A-iii*). By utilizing silence density and MU firing rate CV, we were able to

differentiate recordings without strong slow oscillations from those with strong slow oscillations.

The relationship between cNEs and slow oscillations was investigated by applying the cNE detection algorithm to recordings without strong oscillations in response to DMR during 15 min recordings. Recordings exhibiting low silence density and low CV of the MU firing rate were selected to ensure the absence of strong slow oscillations [n(animals), MGB = 8; A1 = 18; n(recordings), MGB = 13; A1 = 10]. To determine whether cNEs were solely a by-product of slow oscillations, we compared the number of cNEs detected in these recordings against the expected false-positive rate. We found a significantly higher occurrence of cNEs in activity characterized by low silence density and low MU firing rate CV in both MGB [n(cNE) = 3.9 ± 1.0, mean ± SD; $p = 2.4 \times 10^{-4}$, Wilcoxon signed-rank test] and A1 [n(cNE) = 5.2 ± 1.9; $p = 0.002$] when compared with shuffled data (as in Fig. 5). This supports the notion that cNEs are not a by-product of slow oscillations.

Slow oscillations in thalamic and cortical firing rates are commonly observed and can be related to synchronized and desynchronized states of the system (Metherate and Ashe, 1993; Steriade et al., 1993; Cowan and Wilson, 1994; Sanchez-Vives and McCormick, 2000; Hasenstaub et al., 2007). However, the effect of firing rate changes on the information carried by cNEs is not known. Therefore, we tested whether cNE spikes exhibit enhanced information encoding in recordings without strong oscillations in response to the stimulus. The results showed that cNE spike STRFs have higher MI compared with all spikes in both MGB and A1 (Fig. 8*B*), indicating that enhanced information encoding is not specific to synchronized states under slow oscillations. Additionally, a subset of recordings did not show strong slow oscillations in either stimulus-driven or spontaneous activity [n(animals), MGB = 4; A1 = 6; n(recordings), MGB = 5; A1 = 8]. We also examined the stability of cNEs across and within stimulus conditions in these recordings. The majority of cNEs were stable both within and across stimulus conditions (Fig. 8*C*). In summary, cNEs exist in both MGB and A1 without the presence of strong slow oscillations in neural activity. Their enhanced information encoding and stability across stimulus conditions are not due to a special behavior of neurons in synchronized states under slow oscillations.

Discussion

This study aimed to investigate whether the auditory thalamus (MGB) contains cNEs with enhanced information properties, similar to those observed in A1. Our results confirm the presence of cNEs in the MGB, with consistent compositions across various, but especially smaller, bin sizes and stable structures across different stimulus conditions. Importantly, coordinated spikes among cNE member neurons exhibit higher reliability and convey more stimulus-related information than those among individual neurons. Neuronal groups formed by shared firing rate changes to stimuli appear not to be congruent with cNEs. Furthermore, our findings demonstrate that cNEs are not the result of false-positive detections or by-products of slow-state oscillations in anesthetized animals. These findings provide support for the notion that synchronized neuronal ensembles represent a general principle of local organization for information processing in the auditory forebrain.

cNEs are ubiquitous in local circuit organization

Neuronal ensembles were proposed as fundamental units for information processing in the brain (Hebb, 1949; Buzsáki, 2010), supported by evidence of precise temporal coordination in cortical columns (Atencio and Schreiner, 2013; See et al., 2018; Lankarany et al., 2019). Cortical columns consist of neurons with fairly homogeneous properties maintained through intracortical processing and shared afferent input (Mountcastle, 1997). This raises the question of whether cNEs are unique to cortical organization or represent a general organizational and information processing unit along sensory pathways. In the auditory system, reciprocal connectivity exists between the MGB and A1, with convergence of frequency tuning and spectral and temporal modulation preferences, preserving topographic organization in both regions (Miller et al., 2001, 2002; Bartlett and Wang, 2007; Read et al., 2011). Therefore, investigating neuronal coordination in the MGB, where neurons possess similar properties but differ in their organizational and cytoarchitectonic patterns from A1 (Winer, 2010), can provide insights into whether cNEs are general organizational principles of local circuits or specialized units specific to the cortical circuit composition.

We conducted recordings of neuronal activity across multiple isofrequency layers of the MGB and were able to reliably detect cNEs in MGB (Fig. 2). Neurons within the same cNE displayed closer spatial proximity and shared more similar tuning properties (Fig. 5*D*,*E*), indicating functional coherence within cNEs. It is important to note that our recordings were limited to relatively small populations of 10–30 neurons due to the techniques employed. Therefore, the confinement of spatial and frequency tuning properties within cNEs may vary when larger populations with hundreds or thousands of neurons are recorded.

We further demonstrated that the identification of cNEs relies on the temporal coordination among neurons. When the original temporal order among neurons was disrupted through circular shuffling of spike trains, a significantly lower number of cNEs were detected in both the MGB and A1 (Figs. 4*F*, 7*D*). Moreover, the few false-positive cNEs that were identified did not exhibit the properties observed in cNEs identified in the real data, such as stability across different stimulus conditions (Figs. 4*E*, 7*E*). These findings provide strong support for the critical role of temporal coordination in the formation and characterization of cNEs in the auditory thalamus and cortex.

Timescale of cNEs

Previous studies have investigated neuronal synchrony and coordination across widely differing timescales, ranging from a few milliseconds (Lankarany et al., 2019; Shahidi et al., 2019; El-Gaby et al., 2021) to several hundred milliseconds (Miller et al., 2014; Tremblay et al., 2015; Filipchuk et al., 2022). The selection of a specific timescale in these studies was influenced by various factors, including the temporal resolution of the recording methods used, the targeted functional timescale, and the interneuronal distance under investigation. In the context of auditory processing, where information changes rapidly within tens of milliseconds (Rosen, 1992), we specifically chose a temporal resolution of 10 ms. This choice aligns with the timescale at which auditory information operates and holds relevance for synaptic integration. Selecting an appropriate timescale is crucial for future investigations into the functional role of cNEs in synaptic transmission within the auditory thalamocortical system.

We have demonstrated the robustness of cNE identification across different time bin sizes (Fig. 3), which can be attributed to the sparse nature of neural activity. Since most synchronized neuronal firing occurs at frequencies below 10 Hz (O'Connor et al., 2010), the choice of time windows, whether 10 ms or

20 ms, has minimal impact on the observed correlations among neurons. However, it is important to note that cNEs identified with longer time resolutions (hundreds of milliseconds) may significantly differ from those identified with shorter resolutions (tens of milliseconds). Specifically, cNEs identified with larger time bins may falsely include "synchronous" events from bursting or rebound activity rather than from an initial period that dominates the transmission of stimulus-triggered information. Long synchronization windows may also include neurons displaying weaker synchronization within short time windows while potentially de-emphasizing neurons with high temporal precision in synchrony (Fig. 3*D*). Hence, the chosen temporal resolution influences the composition and properties of cNEs, emphasizing the importance of selecting the appropriate timescale for studying neural ensembles.

Stability of cNEs for spontaneous and evoked activity

Our study revealed that a significant proportion of cNEs (55% in MGB and 76% in A1) maintained a consistent composition during both spontaneous and sensory-evoked neural activity (Figs. 4*E*, 7*E*). This suggests that cNEs generally represent stable configurations within local circuits that can manifest independently of stimulus-driven synchrony. These findings align with previous research demonstrating similarities between patterns observed in spontaneous and stimulus-driven activity (Luczak et al., 2009). Moreover, the similarity between MGB and A1 cNEs indicates that functional network units are not limited to cortical organization but likely exist as a common modality across multiple stages of the sensory pathway.

cNEs enhance stimulus encoding

Considering that cNEs were observed in both spontaneous and stimulus-driven activity, some argue that they are merely a reflection of background activity and not involved in stimulus encoding and even potentially impairing it (Zohary et al., 1994; Abbott and Dayan, 1999; Jermakowicz et al., 2009). Contrary to this notion, our observations revealed that cNE spikes exhibit a higher SNR and convey more information per spike when compared with the entire spike train (Fig. 6*B*,*C*). This suggests that cNE events are more stimulus selective than the contributing neurons (See et al., 2021) and exhibit a more reliable response to the stimulus features represented by the cNE STRF. The stable connectivity pattern revealed by spontaneous, intrinsic activity likely reveals aspects that have been imprinted by extensive experience and the behavioral relevance of the associated functional preferences.

Additionally, we observed an enhanced information encoding in cNE groups and cNE spikes when compared with non-cNE groups or coincident spikes, with control of the total number of neurons in the groups (Fig. 6*B*,*C*). This observation suggests that the information increase relies on the coordination among cNE member neurons, rather than being a simple result of independent population coding (deCharms, 1998; Hatsopoulos et al., 1998).

Correlated spikes can enhance the transmission of salient auditory information by synchronously converging on their targets (Stevens and Zador, 1998; Zandvakili and Kohn, 2015). Additionally, neurons exhibit a multiplexed nature of stimulus encoding, where spikes from the same neuron can carry information related to distinct stimulus aspects (Walker et al., 2011; Lankarany et al., 2019; See et al., 2021). The function of cNEs may involve selectively choosing spikes from member neurons that are most relevant for a specific target information and enhancing information propagation while excluding functionally irrelevant spikes of the same neurons. This mechanism significantly improves both the robustness and capacity of information encoded within a population of neurons (Walker et al., 2011; See et al., 2021). Thus, the presence of cNEs and their coordination within a neuronal population can facilitate efficient information processing and transmission in the auditory system. Future studies involving simultaneous recordings from two stations along the auditory pathway will be necessary to test this hypothesis.

cNE formation does not depend on strong slow oscillations

Slow oscillations are commonly observed in neural activity during anesthesia (Chauvette et al., 2011; Dasilva et al., 2021) and have been shown to influence stimulus encoding (Pachitariu et al., 2015). Concerns have been raised regarding whether cNEs are solely a result of anesthesia-induced synchrony. However, our research findings refute this notion. We focused on a distinct timescale of synchronization unrelated to anesthesia-induced slow oscillations and successfully detected cNEs in recordings without strong slow oscillations. These cNEs exhibited stable structures and enhanced information properties, indicating that they are not solely a by-product of anesthesia-induced synchrony. While we ruled out slow oscillations as the primary force underlying cNE formation, it is important to consider their potential interaction with other oscillatory activity, such as gamma rhythms (Oberto et al., 2022). Further research is needed to explore the interplay between cNEs and different types of brain oscillations.

References

Abbott LF, Dayan P (1999) The effect of correlated variability on the accuracy of a population code. Neural Comput 11:91–101.

Anderson LA, Linden JF (2011) Physiological differences between histologically defined subdivisions in the mouse auditory thalamus. Hear Res 274:48–60.

Aschauer DF, Eppler JB, Ewig L, Chambers AR, Pokorny C, Kaschube M, Rumpel S (2022) Learning-induced biases in the ongoing dynamics of sensory representations predict stimulus generalization. Cell Rep 38: 110340.

Atencio CA, Schreiner CE (2008) Spectrotemporal processing differences between auditory cortical fast-spiking and regular-spiking neurons. J Neurosci 28:3897–3910.

Atencio CA, Schreiner CE (2010) Laminar diversity of dynamic sound processing in cat primary auditory cortex. J Neurophysiol 103:192–205.

Atencio CA, Schreiner CE (2013) Auditory cortical local subnetworks are characterized by sharply synchronous activity. J Neurosci 33:18503–18514.

Baeg EH, Kim YB, Huh K, Mook-Jung I, Kim HT, Jung MW (2003) Dynamics of population code for working memory in the prefrontal cortex. Neuron 40:177–188.

Bartlett EL (2013) The organization and physiology of the auditory thalamus and its role in processing acoustic features important for speech perception. Brain Lang 126:29–48.

Bartlett EL, Wang X (2007) Neural representations of temporally modulated signals in the auditory thalamus of awake primates. J Neurophysiol 97: 1005–1017.

Bathellier B, Ushakova L, Rumpel S (2012) Discrete neocortical dynamics predict behavioral categorization of sounds. Neuron 76:435–449.

Bizley JK, Walker KMM, King AJ, Schnupp JWH (2010) Neural ensemble codes for stimulus periodicity in auditory cortex. J Neurosci 30:5078–5091.

Boucly CJ, Pompili MN, Todorova R, Leroux EM, Wiener SI, Zugaro M (2022) Flexible communication between cell assemblies and 'reader' neurons. bioRxiv:2009–2022.

Brosch M, Schreiner CE (1999) Correlations between neural discharges are related to receptive field properties in cat primary auditory cortex. Eur J Neurosci 11:3517–3530.

Buzsáki G (2010) Neural syntax: cell assemblies, synapsembles, and readers. Neuron 68:362–385.
Carrillo-Reid L, Miller JEK, Hamm JP, Jackson J, Yuste R (2015) Endogenous sequential cortical activity evoked by visual stimuli. J Neurosci 35:8813–8828.
Chamberland S, Yang HH, Pan MM, Evans SW, Guan S, Chavarha M, Yang Y, Salesse C, Wu H, Wu JC (2017) Fast two-photon imaging of subcellular voltage dynamics in neuronal tissue with genetically encoded indicators. Elife 6:e25690.
Chauvette S, Crochet S, Volgushev M, Timofeev I (2011) Properties of slow oscillation during slow-wave sleep and anesthesia in cats. J Neurosci 31:14998–15008.
Contreras D, Timofeev I, Steriade M (1996) Mechanisms of long-lasting hyperpolarizations underlying slow sleep oscillations in cat corticothalamic networks. J Physiol 494:251–264.
Cowan RL, Wilson CJ (1994) Spontaneous firing patterns and axonal projections of single corticostriatal neurons in the rat medial agranular cortex. J Neurophysiol 71:17–32.
D'amour JA, Froemke RC (2015) Inhibitory and excitatory spike-timing-dependent plasticity in the auditory cortex. Neuron 86:514–528.
Dan Y, Alonso JM, Usrey WM, Reid RC (1998) Coding of visual information by precisely correlated spikes in the lateral geniculate nucleus. Nat Neurosci 1:501–507.
Dasilva M, Camassa A, Navarro-Guzman A, Pazienti A, Perez-Mendez L, Zamora-López G, Mattia M, Sanchez-Vives MV (2021) Modulation of cortical slow oscillations and complexity across anesthesia levels. Neuroimage 224:117415.
deCharms RC (1998) Information coding in the cortex by independent or coordinated populations. Proc Natl Acad Sci U S A 95:15166–15168.
deCharms RC, Merzenich MM (1996) Primary cortical representation of sounds by the coordination of action-potential timing. Nature 381:610–613.
Domanski APF, Kucewicz MT, Russo E, Tricklebank MD, Robinson ESJ, Durstewitz D, Jones MW (2023) Distinct hippocampal-prefrontal neural assemblies coordinate memory encoding, maintenance, and recall. Curr Biol 33:1220–1236.
Ebrahimi S, Lecoq J, Rumyantsev O, Tasci T, Zhang Y, Irimia C, Li J, Ganguli S, Schnitzer MJ (2022) Emergent reliability in sensory cortical coding and inter-area communication. Nature 605:713–721.
Eggermont JJ (2000) Sound-induced synchronization of neural activity between and within three auditory cortical areas. J Neurophysiol 83:2708–2722.
El-Gaby M, Reeve HM, Lopes-dos-Santos V, Campo-Urriza N, Perestenko PV, Morley A, Strickland LAM, Lukács IP, Paulsen O, Dupret D (2021) An emergent neural coactivity code for dynamic memory. Nat Neurosci 24:694–704.
Escabí MA, Schreiner CE (2002) Nonlinear spectrotemporal sound analysis by neurons in the auditory midbrain. J Neurosci 22:4114–4131.
Filipchuk A, Schwenkgrub J, Destexhe A, Bathellier B (2022) Awake perception is associated with dedicated neuronal assemblies in the cerebral cortex. Nat Neurosci 25:1327–1338.
Harris KD, Csicsvari J, Hirase H, Dragoi G, Buzsáki G (2003) Organization of cell assemblies in the hippocampus. Nature 424:552–556.
Hasenstaub A, Sachdev RNS, McCormick DA (2007) State changes rapidly modulate cortical neuronal responsiveness. J Neurosci 27:9607–9622.
Hatsopoulos NG, Ojakangas CL, Paninski L, Donoghue JP (1998) Information about movement direction obtained from synchronous activity of motor cortical neurons. Proc Natl Acad Sci U S A 95:15706–15711.
Hebb DO (1949) *The organization of behavior*. New York, NY: John Wiley & Son.
Homma NY, Hullett PW, Atencio CA, Schreiner CE (2020) Auditory cortical plasticity dependent on environmental noise statistics. Cell Rep 30:4445–4458.e5.
Imaizumi K, Priebe NJ, Crum PA, Bedenbaugh PH, Cheung SW, Schreiner CE (2004) Modular functional organization of cat anterior auditory field. J Neurophysiol 92:444–457.
Ince RAA, Panzeri S, Kayser C (2013) Neural codes formed by small and temporally precise populations in auditory cortex. J Neurosci 33:18277–18287.
Jermakowicz WJ, Chen X, Khaytin I, Bonds AB, Casagrande VA (2009) Relationship between spontaneous and evoked spike-time correlations in primate visual cortex. J Neurophysiol 101:2279–2289.
Konorski J (1948) *Conditioned reflexes and neuron organization*. Cambridge, MA: Cambridge University Press.
Kreiter AK, Singer W (1996) Stimulus-dependent synchronization of neuronal responses in the visual cortex of the awake macaque monkey. J Neurosci 16:2381–2396.
Lankarany M, Al-Basha D, Ratté S, Prescott SA (2019) Differentially synchronized spiking enables multiplexed neural coding. Proc Natl Acad Sci U S A 116:10097–10102.
Laubach M, Wessberg J, Nicolelis MAL (2000) Cortical ensemble activity increasingly predicts behaviour outcomes during learning of a motor task. Nature 405:567–571.
Léger JF, Stern EA, Aertsen A, Heck D (2005) Synaptic integration in rat frontal cortex shaped by network activity. J Neurophysiol 93:281–293.
Lopes-dos-Santos V, Ribeiro S, Tort ABL (2013) Detecting cell assemblies in large neuronal populations. J Neurosci Methods 220:149–166.
Luczak A, Barthó P, Harris KD (2009) Spontaneous events outline the realm of possible sensory responses in neocortical populations. Neuron 62:413–425.
Marchenko VA, Pastur LA (1967) Distribution of eigenvalues for some sets of random matrices. Mat Sb 114:507–536.
Merzenich MM, Knight PL, Roth GL (1975) Representation of cochlea within primary auditory cortex in the cat. J Neurophysiol 38:231–249.
Metherate R, Ashe JH (1993) Nucleus basalis stimulation facilitates thalamocortical synaptic transmission in the rat auditory cortex. Synapse 14:132–143.
Miller JEK, Ayzenshtat I, Carrillo-Reid L, Yuste R (2014) Visual stimuli recruit intrinsically generated cortical ensembles. Proc Natl Acad Sci U S A 111:E4053–E4061.
Miller LM, Escabí MA, Read HL, Schreiner CE (2001) Functional convergence of response properties in the auditory thalamocortical system. Neuron 32:151–160.
Miller LM, Escabí MA, Read HL, Schreiner CE (2002) Spectrotemporal receptive fields in the lemniscal auditory thalamus and cortex. J Neurophysiol 87:516–527.
Miller LM, Recanzone GH (2009) Populations of auditory cortical neurons can accurately encode acoustic space across stimulus intensity. Proc Natl Acad Sci U S A 106:5931–5935.
Miller LM, Schreiner CE (2000) Stimulus-based state control in the thalamocortical system. J Neurosci 20:7011–7016.
Mochol G, Hermoso-Mendizabal A, Sakata S, Harris KD, De La Rocha J (2015) Stochastic transitions into silence cause noise correlations in cortical circuits. Proc Natl Acad Sci U S A 112:3529–3534.
Mogensen H, Norrlid J, Enander JMD, Wahlbom A, Jörntell H (2019) Absence of repetitive correlation patterns between pairs of adjacent neocortical neurons in vivo. Front Neural Circuits 13:1–11.
Morel A, Rouiller E, de Ribaupierre Y, de Ribaupierre F (1987) Tonotopic organization in the medial geniculate body (MGB) of lightly anesthetized cats. Exp Brain Res 69:24–42.
Mountcastle VB (1997) The columnar organization of the neocortex. Brain 120:701–722.
Neske GT (2016) The slow oscillation in cortical and thalamic networks: mechanisms and functions. Front Neural Circuits 9:1–25.
Niessing J, Friedrich RW (2010) Olfactory pattern classification by discrete neuronal network states. Nature 465:47–52.
Oberto VJ, Boucly CJ, Gao H, Todorova R, Zugaro MB, Wiener SI (2022) Distributed cell assemblies spanning prefrontal cortex and striatum. Curr Biol 32:1–13.
O'Connor DH, Peron SP, Huber D, Svoboda K (2010) Neural activity in barrel cortex underlying vibrissa-based object localization in mice. Neuron 67:1048–1061.
Pachitariu M, Lyamzin DR, Sahani M, Lesica NA (2015) State-dependent population coding in primary auditory cortex. J Neurosci 35:2058–2073.
Pachitariu M, Sridhar S, Stringer C (2023) Solving the spike sorting problem with Kilosort. bioRxiv:2023.01.07.523036.
Paninski L, Shoham S, Fellows MR, Hatsopoulos NG, Donoghue JP (2004) Superlinear population encoding of dynamic hand trajectory in primary motor cortex. J Neurosci 24:8551–8561.
Peyrache A, Benchenane K, Khamassi M, Wiener SI, Battaglia FP (2010) Principal component analysis of ensemble recordings reveals cell assemblies at high temporal resolution. J Comput Neurosci 29:309–325.
Polley DB, Read HL, Storace DA, Merzenich MM (2007) Multiparametric auditory receptive field organization across five cortical fields in the albino rat. J Neurophysiol 97:3621–3638.

Qiu A, Schreiner CE, Escabí MA (2003) Gabor analysis of auditory midbrain receptive fields: spectro-temporal and binaural composition. J Neurophysiol 90:456–476.
Read HL, Nauen DW, Escabí MA, Miller LM, Schreiner CE, Winer JA (2011) Distinct core thalamocortical pathways to central and dorsal primary auditory cortex. Hear Res 274:95–104.
Rosen S (1992) Temporal information in speech: acoustic, auditory and linguistic aspects. Philos Trans R Soc Lond Ser B Biol Sci 336:367–373.
Sanchez-Vives MV, McCormick DA (2000) Cellular and network mechanisms of rhythmic recurrent activity in neocortex. Nat Neurosci 3: 1027–1034.
See JZ, Atencio CA, Sohal VS, Schreiner CE (2018) Coordinated neuronal ensembles in primary auditory cortical columns. Elife 7:1–33.
See JZ, Homma NY, Atencio CA, Sohal VS, Schreiner CE (2021) Information diversity in individual auditory cortical neurons is associated with functionally distinct coordinated neuronal ensembles. Sci Rep 11:4064.
Shahidi N, Andrei AR, Hu M, Dragoi V (2019) High-order coordination of cortical spiking activity modulates perceptual accuracy. Nat Neurosci 22:1148–1158.
Smith PH, Uhlrich DJ, Manning KA, Banks MI (2012) Thalamocortical projections to rat auditory cortex from the ventral and dorsal divisions of the medial geniculate nucleus. J Comp Neurol 520:34–51.
Steinmetz NA, et al. (2021) Neuropixels 2.0: a miniaturized high-density probe for stable, long-term brain recordings. Science 372:eabf4588.
Steriade M, McCormick DA, Sejnowski TJ (1993) Thalamocortical oscillations in the sleeping and aroused brain. Science 262:679–685.
Stevens CF, Zador AM (1998) Input synchrony and the irregular firing of cortical neurons. Nat Neurosci 1:210–217.
Theunissen FE, Sen K, Doupe AJ (2000) Spectral-temporal receptive fields of nonlinear auditory neurons obtained using natural sounds. J Neurosci 20: 2315–2331.
Tremblay S, Pieper F, Sachs A, Martinez-Trujillo J (2015) Attentional filtering of visual information by neuronal ensembles in the primate lateral prefrontal cortex. Neuron 85:202–215.
Wahlbom A, Mogensen H, Jörntell H (2021) Widely different correlation patterns between pairs of adjacent thalamic neurons in vivo. Front Neural Circuits 15:1–10.
Walker KMM, Bizley JK, King AJ, Schnupp JWH (2011) Multiplexed and robust representations of sound features in auditory cortex. J Neurosci 31:14565–14576.
Wills TJ, Lever C, Cacucci F, Burgess N, O'Keefe J (2005) Attractor dynamics in the hippocampal representation of the local environment. Science 308: 873–876.
Winer JA (2010) Neurochemical organization of the medial geniculate body and auditory cortex. In: *The auditory cortex*, pp 209–234. Springer.
Winer JA, Miller LM, Lee CC, Schreiner CE (2005) Auditory thalamocortical transformation: structure and function. Trends Neurosci 28:255–263.
Yoshida T, Ohki K (2020) Natural images are reliably represented by sparse and variable populations of neurons in visual cortex. Nat Commun 11:872.
Yuste R (2015) From the neuron doctrine to neural networks. Nat Rev Neurosci 16:487–497.
Zandvakili A, Kohn A (2015) Coordinated neuronal activity enhances corticocortical communication. Neuron 87:827–839.
Zohary E, Shadlen MN, Newsome WT (1994) Correlated neuronal discharge rate and its implications for psychophysical performance. Nature 370: 140–143.